Departamento de Física e Astronomia da Faculdade de Ciências da Universidade do Porto

Optical fiber sensor fabrication using a CO_2 laser

This M.Sc. thesis was conducted under the supervision of

Prof. Dr. Orlando José Reis Frazão

Invited Assistant Professor at the Departamento de Física e Astronomia da Faculdade de Ciências da Universidade do Porto and Senior Researcher at INESC-TEC

and under the co-supervision of

Prof. Dr. Manuel Joaquim Bastos Marques

Assistant Professor at the Departamento de Física e Astronomia da Faculdade de Ciências da Universidade do Porto and Senior Researcher at INESC-TEC

Tiago Jorge Mendes Martins

2015

Acknowledgements

This dissertation is the result of a number of valuable contributions, without which it would not have been possible to accomplish all the work developed during my thesis. To those who contributed a word of appreciation is due.

To my supervisor, Dr. Orlando José Reis Frazão, for introducing me to an investigation environment and proposing such an interesting and challenging project, trusting me with the responsibility to harness the mighty power of the CO_2 laser for good. His willingness to help was a constant throughout the time devoted to this endeavor, never forgetting his amazing "magical touch" in the laboratory to solve the seemingly impossible problems I had to face. For his encouragement and dedication, as well as spirited conversations, I am grateful.

To my co-supervisor, Prof. Manuel Joaquim Bastos Marques, for pitching in with his immense knowledge and skills as an experimentalist and for being always available to find that missing piece, whether in the setup or in the attempt to explain some of the results in light of physical principles.

To the collaborators of INESC-TEC, more precisely to those working at the Center for Applied Photonics (CAP), for easing my entrance in an environment of advanced research by showing they were willing to support me and share some of their time and experience in order for me to improve my own work.

To André Delgado Gomes and Vítor Amorim for developing the LabVIEW routine responsible for controlling the motorized stages used for taper fabrication, crucial in obtaining quality devices. A special thanks to André for tirelessly trying to work out some compatibility problems between the operating system and the installed software.

To those who shared with me the hardships but also the deep satisfaction that come from studying physics and trying to make our contribution to its development. Some of the people I had the pleasure to get to know deserve to be acknowledged, especially my fellow soon-to-be masters in Physics, Pedro, Tenessa and Daniel.

To INESC-TEC and the Physics and Astronomy Department of the Faculty of Sciences of the University of Porto for the technical support and for the opportunity granted to students who intend to further their formation and to make science an important part of their lives.

Lastly, to my parents for putting up with some moody replies when the pressure tightened and for always having my back and never doubting that I could do what I set as a goal for myself.

Abstract

Optical fiber sensing relies on a myriad of devices, such as tapers, fiber Bragg gratings (FBGs) and long period gratings (LPGs), to claim its rightful place as one of the most fertile and promising areas of research in the field of applied physics. This dissertation results from the work developed for a M.Sc. project devoted to studying in detail the fabrication of tapers relying on a high-power CO_2 laser radiation source and its use as sensors.

The physical principle behind the use of tapers as sensors is explained, highlighting how interference is created, approaching a Mach-Zehnder-like interferometer (MZI), and how the interaction between light traveling along the tapered region of the fiber and the surrounding environment takes place and can be monitored. A rather complete state-of-the-art presenting sensing configurations involving tapers is included. The control of the taper shape and the interaction between CO_2 laser radiation and the optical fiber are investigated.

The influence of the fabrication parameters on the tapers shapes and transmission spectra is examined and efforts are made towards optimizing the taper fabrication process and meet a compromise between low power losses and a sharp interference pattern. The potential of these devices for sensing purposes is preliminarily evaluated and the reproducibility of the fabrication setup assessed.

A simple sensing configuration based on a single long taper is tested to monitor temperature, strain and curvature. A strain and curvature-independent temperature sensor is also proposed.

Keywords: CO_2 laser, optical fiber sensor, taper, interferometer

Resumo

Os sensores em fibra óptica compreendem um vasto conjunto de dispositivos, tais como *tapers*, redes de Bragg em fibra e redes de período longo. As potencialidades associadas à utilização destes sensores elevam a investigação desenvolvida em torno das fibras ópticas ao estatuto de um dos campos mais férteis e promissores no âmbito da física aplicada. Esta dissertação resulta do trabalho desenvolvido para um projecto de mestrado dedicado ao estudo detalhado da fabricação de *tapers* recorrendo a um laser de CO_2 e do seu uso como sensores.

O princípio físico por detrás da utilização dos *tapers* como sensores é explicado, sendo destacado o mecanismo que conduz à criação de interferência na fibra óptica, aproximando-se este dispositivo de um configuração interferométrica de Mach-Zehnder, bem como a forma como a interacção entre a luz que viaja ao longo do *taper* e o meio envolvente se desenrola e pode ser monitorizada.

A influência dos parâmetros de fabricação na forma dos *tapers* e no seu espectro de transmissão é examinada e esforços são desenvolvidos no sentido de optimizar o processo de fabricação e alcançar um compromisso entre baixas perdas de potência e padrões de interferência com franjas pronunciadas, resultado de interferência significativa ao longo do *taper*. O potencial destes dispositivos como sensores é alvo de uma avaliação preliminar e a reprodutibilidade da montagem para fabricação é averiguada.

Uma configuração simples incluindo apenas um *taper* longo é testada para monitorização de temperatura, tensão mecânica e curvatura. Um sensor de temperatura independente da tensão mecânica e da curvatura é, também, proposto.

Palavras-chave: Laser de CO_2, sensor em fibra óptica, *taper*, interferómetro

Contents

List of figures

List of tables

Nomenclature

RI – Refractive Index
FBG – Fiber Bragg Grating
UV – Ultraviolet
LPG – Long Period Grating
MZI – Mach-Zehnder Interferometer
MI – Michelson Interferometer
FPI – Fabry-Perot Interferometer
DCF – Double-Core Fiber
SCF – Single-Core Fiber
FSR – Free Spectral Range
HOT – Holographic Optical Tweezers
CQED – Cavity Quantum Electrodynamics
IR – Infrared
OSA – Optical Spectrum Analyzer
PWM – Pulse Width Modulation
PC – Personal Computer
SMC – System Management Controller
SD – Speed Differential
SM – Speed Magnitude
ETI – Exposure Time Interval
PCF – Photonic Crystal Fiber
SMF – Single-mode Fiber
MOF – Microstructured Optical Fiber
SFBG – Superstructure Fiber Bragg Grating
TFBG – Tilted Fiber Bragg Grating
MMF – Multi-mode Fiber

1. Introduction

1.1 Motivation

The mysteries of light have triggered human curiosity way beyond the scope of science. From painting to literature, and never forgetting cinema and photography, light, shadow and colors are used to create new universes, to shed new meaning on existence. The manifestations of the metaphysics of light constitute evidence of its importance in our life, but also of an intrinsic nature difficult to decipher for many. Since Newton first saw and understood the spectrum of visible light, and then Fraunhofer studied the spectral lines of the sun, a new way of seeing made possible to unveil some of the most powerful hidden secrets of the universe. Daily life also benefited from a deeper knowledge of the nature of light, from communication to energy generation. Light-based technology is growing in importance and the investment channeled to this particular area has known consistent increase over the last years.

Optical fiber communication plays an instrumental role in connecting the entire world allowing for a fast and efficient exchange of information and ideas. Some of the advantages of optical fibers are worth mentioning such as its reduced dimensions, good mechanical performance and low cost. Sensors based on these structures are very enticing and appealing to work with since they are embedded in the communication channel. The operating principle relies on the interaction established between light traveling along the fiber and both the sensing device as well as the surrounding environment. Such interaction can be monitored at long distances since the vehicle conveying information is light.

Tapers are thinned portions of an optical fiber. The resulting changes in the profile of the fiber core/cladding interface are responsible for coupling light out from the core into the cladding. The tapered portion of a fiber can then be seen has a Mach-Zehnder interferometer (MZI). Light traveling along the cladding is more susceptible to changes in external parameters such as temperature and curvature. The simple physical principle behind the workings of the taper as a sensor makes it an appealing device that can be easily operated and monitored. The fabrication process can also be quite straight-forward to implement, especially when compared to more difficult techniques for fiber Bragg grating (FBG) and long period grating (LPG) fabrication. The possibility of learning more about

the specifics of taper fabrication is also an attractive aspect of this work, particularly given the inclusion of a CO_2 laser. The assembly procedure of the laser system and the efforts leading to the optimization of the fabrication process represent an incredible and fulfilling experience.

Besides the simple physical principle and swift fabrication technique, tapers can upstage other sensing devices when it comes to physical parameter discrimination, without compromising the sensitivity.

This work also poses an opportunity to plunge deeper into other phenomena that take place when light propagates along an optical fiber while the latter is being actively changed. A better understanding of how radiation and matter interact can be achieved trying to characterize the changes in the fiber structure and shape when infra-red (IR) laser radiation shines upon it.

The main goal is to optimize the taper fabrication process and characterize the resulting devices as sensors of temperature, strain and curvature, hopefully being able to discriminate between physical parameters for a more precise determination of the influence of a single external parameter on the characteristics of the light interacting with said device.

1.2 Objectives

- Engage in a committed effort to assemble a complete experimental setup for taper fabrication relying on a CO_2 laser.

- Study the interaction between the CO_2 laser radiation and the material of the optical fiber, namely in what concerns the changes in its inner structure leading to refractive index modulation.

- Optimize the taper fabrication process, selecting the most adequate values for the fabrication parameters, such as CO_2 laser power and the motorized stages speed, in order to achieve a compromise between low power losses and effective interference along the tapered region.

- Investigate the behavior of the fabricated interferometric tapers as sensors of temperature, strain and curvature.

1.3 Organization of the dissertation

This dissertation is divided into six chapters. A more detailed description of their contents follows.

Chapter 1 presents the motivation for this work and some of the main goals expected to be achieved while developing it.

Chapter 2 contains a comprehensive state-of-the-art concerning the use of tapers in sensing devices. The physical principle behind the operation of the taper as a sensor is described. The possibility of controlling the taper shape with a setup including PC controlled motorized stages is discussed. Investigations regarding the result of the CO_2 laser interaction with the optical fiber are included, namely the changes in the fiber structure and the consequent refractive index modulation.

Chapter 3 encompasses a description of the experimental setup designed and assembled for taper fabrication. Tapers are fabricated using weights attached to the fiber, responsible for increasing mechanical stress and furthering the potentialities of the fabrication technique. The analysis of the results is focused on the time evolution of the taper shape and transmission spectrum. The latter allowed for a preliminary evaluation of the taper potential as a sensor. The light reflected at the taper is also scrutinized to understand how much it accounts for the overall power losses.

Chapter 4 summarizes the efforts towards the optimization of the fabrication setup after the inclusion of motorized stages. Different values for laser power and for the velocity of each stage are considered and the resulting taper shapes and transmission spectra inspected. A compromise between power losses and an effective light interference along the taper is met. Reproducibility is assessed using the values of the fabrication parameters corresponding to such compromise.

Chapter 5 includes the characterization of the fabricated tapers as sensors of temperature, strain and curvature. The transmission spectra evolution is evaluated in terms of the variation of the wavelengths of the resonant loss peaks as well as of the corresponding power as the external parameters change. The sensitivities are calculated and physical parameter discrimination achieved.

Chapter 6 features some concluding remarks concerning the work developed and some open-ended possibilities for future work.

1.4 Outputs

T. J. M. Martins, O. Frazão, M. B. Marques, *Strain and curvature-independent temperature sensor based on an interferometer taper fabricated with CO_2 laser*, Microwave and Optical Technology Letters.

2. State-of-the-art

2.1 Tapers as sensors

The potential of optical fiber-based devices for sensing has been explored for several decades and met a significant boost when tapers were brought forth, initially as beam expanders **[1, 2]**, which would make possible for light to be coupled in or out of the fiber. As light travels through a tapered region of the fiber, it is no longer confined to the fundamental mode of the core as a portion of its energy propagates as higher-order modes allowed in the cladding and then out of the fiber. In fact, the large diameter of the cladding (when compared to the typical dimensions of the core) renders this part of the fiber highly multimode. When light is guided through the cladding, the effective refractive index that characterizes its propagation becomes a more complex object of study since it depends on the mode under consideration and also on the characteristics of the surrounding environment. Even as early as the date of publication of these first articles, the notion that the diameter as well as the length of the taper would have a significant impact on its performance as a coupler was present, as different parameters originated different coupling ratios.

The awareness of the influence of external parameters on light propagation as a higher-order mode along the cladding set in motion the wheels for the development of the first refractive index (RI) sensors based on tapers **[3-5].** Variations in the RI of the environment change the way light is coupled from the cladding to the exterior, in particular, the power that is coupled out and, therefore, no longer detected at the output of the fiber. The coupling coefficient is noticeably affected by changes in the external RI **[3, 4]**. A linear relation between the wavelength corresponding to one of the loss peaks and the inverse of the square root of the difference between the squared RIs of the fiber and of the exterior is also found **[4]**. A more detailed study was carried out as the behavior of the relation between output power and RI was analyzed for different taper lengths **[5]**. The region of maximum sensitivity changes but the results predominantly show that the main variations in the output power occur for values of the RI relatively close to the RI of silica (~1.44), which is the major component of optical fibers; outside a given range (depending on the taper length, but never spreading more than one hundredth of the value for which power is

minimum, close to 1.44), output power is almost constant. These results agree with Fresnel equations for power transmission: as the difference in refractive index between two neighboring media decreases, the power transmitted increases, leading to a smaller value detected at the output of the fiber. Nevertheless, at least for one of the attempted taper lengths, a promising linear relation between power and RI was obtained for RI smaller than that of silica. The possibility of tapers as attenuators and sensors is reinforced: depending on the refractive index of the surrounding environment, significant changes in the output power are obtained, meaning that placing the taper in a medium with matching RI may provide attenuation in the output signal; the approximately linear relation previously made reference to can be used for a sensor.

More complex structures were later obtained by inscribing fiber Bragg gratings (FBG) in tapered fibers **[6-8]**. These devices combine FBGs, produced by shining ultraviolet (UV) light through a phase mask on a photosensitive fiber, with a taper produced in the exact place where the FBG is later inscribed. As a consequence, a strain gradient is created along the fiber, messing with the well-behaved profile of a standard grating consisting of a RI modulation with constant spatial period. The final product is a chirped Bragg grating differing from the original FBG in the bandwidth, which becomes wider. The usual profile is linear chirp but can be changed by resorting to different taper shapes. These sensors can be used to solve an ever-present problem in optical fiber sensing: cross-sensitivity. When the output of a given sensing device is being monitored, it is quite a challenge to isolate the variations emerging from temperature, strain, bending or RI. The development of sensors intrinsically insensitive to some of these parameters is of the essence. Chirped Bragg gratings turn out to be temperature insensitive and, therefore, useful for strain monitoring [**7].** Other attempts at solving cross-sensitivity were considered, resorting to other structures such as LPGs and FBGs **[9-13]**.

A theoretical model for the shape of tapers was proposed by Birks *et al.* **[14]**, allowing the establishment of a clearer connection between the final shape of a taper and the parameters used in its fabrication, namely the variation of the area under the action of the main shaping element (hot zone), which could be a flame torch (predominant technique

in the early stages of taper development), an arc-induced electrical discharge or a CO_2 laser **[15]** (current dominant techniques). Several shapes can be obtained through a linear evolution of the hot zone length (which ensures an easy experimental implementation): linear, exponential or abrupt taper (short transition region). One of the most interesting results is the adiabaticity criterion, establishing conditions for minimum coupling from the core fundamental mode to cladding excited modes. In order to minimize coupling, the transition length should be large so to reach a slow rate of decrease of the fiber radius. The relevance of this deeper understanding of how to control the shape of a taper is undeniably of interest for the improvement of sensing devices and the possibility of entering new fields like micro or nanofiber fabrication.

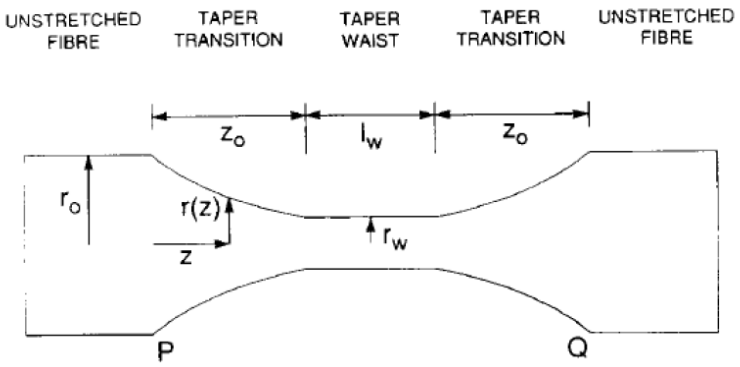

Figure 2.1.1 - Typical shape of a taper [14].

The previously mentioned use of tapers as sensors was based on simply evaluating the dependence of the output power on external parameters like strain, temperature and RI.

More recently, devices based on interferometry have taken over, whether being Mach-Zender (MZI), Michelson (MI) or Fabry-Perot (FPI) interferometers. For a Mach-Zender-like sensor **[16-24],** usually one of two approaches is taken: either a device composed of two short tapers in series or a single, narrow and long taper. In the first case, part of the light is coupled out of the core into the cladding in the first taper. As a consequence, two beams will propagate along the fiber with different RIs. While the RI of the core remains essentially unchanged despite hypothetical variations of external

parameters like temperature T, strain ε or RI, the RI of the cladding is much more sensitive to said variations. As light approaches the second taper, the portion that was previously coupled out to the cladding is coupled back into the core. In this case the length of interaction is the distance L between the two tapers. In the second case, the dynamics is similar: light is coupled out from the core to the cladding and back to the core at the beginning and at the end of the taper, respectively, and the length of the interaction equals the length of the taper. The sensor is based on the wavelength shift observed in the interference pattern as a result of external variations in the quantities that may impact on the effective RI that characterizes light propagation along the core. The interference pattern for two beams of intensities I_1 and I_2 , with a phase difference Δφ obeys the relation

$$I = I_1 + I_2 + 2\sqrt{I_1 I_2}\cos(\Delta\varphi)\,. \tag{2.1.1}$$

The phase difference between the core mode and the *m*th cladding mode is

$$\Delta\varphi^m = \frac{2\pi L}{\lambda}\Delta n_{eff}^m = \frac{2\pi L}{\lambda}\left(n_{eff,core}(RI) - n_{eff,cladding}^m(RI)\right), \tag{2.1.2}$$

where $n_{eff,cladding}^m$ is the effective RI of the *m*th mode of the cladding and $n_{eff,core}$ is the effective RI of the core, both functions of the external RI (which can suffer variations due to changes in temperature, for example), but exhibiting distinct dependences; λ is the radiation wavelength. Considering the wavelength that corresponds to a phase difference that minimizes I ($\Delta\varphi^m = (2n+1)\pi$),

$$\lambda^n = \frac{2L}{(2n+1)}\Delta n_{eff}^m(\xi + \Delta\xi)\,, \tag{2.1.3}$$

where ξ is the external parameter impacting on the actual value of the effective RI difference Δn_{eff}^m . An expression for the dependence of the wavelength shift as a function of

$\Delta\xi$ can be derived, assuming it takes relatively small values. Resorting to a first order approximation,

$$\Delta n_{eff}^{m}(\xi+\Delta\xi) \approx \Delta n_{eff}^{m}(\xi) + \left[\frac{\partial \Delta n_{eff}^{m}}{\partial \xi}\right]_{\xi+\Delta\xi=\xi} (\xi+\Delta\xi-\xi), \tag{2.1.4}$$

where $\Delta n_{eff}^{m}(\xi)$ can be thought of as the effective RI difference when no variation takes place and $\left[\frac{\partial \Delta n_{eff}^{m}}{\partial \xi}\right]_{\xi+\Delta\xi=\xi} \equiv s$ is the sensitivity, a measure of the impact of the variation $\Delta\xi$ on the effective RI difference. Finally, substituting (2.1.4) into (2.1.3),

$$\lambda^{n} \approx \frac{2L}{(2n+1)}\left[\Delta n_{eff}^{m}(\xi) + s\Delta\xi\right] = \lambda_{0}^{n} + \frac{2L}{(2n+1)} s\Delta\xi. \tag{2.1.5}$$

Rearranging (2.1.5), a very pleasant and illustrative relation is obtained

$$\Delta\lambda^{n} \approx \frac{2L}{(2n+1)} s\Delta\xi, \tag{2.1.6}$$

highlighting the possibility of arriving at an enticing approximately linear relation between wavelength shift and the external parameter variation, mediated by the sensitivity of the sensor. A new expression for the sensitivity can be written to include L,

$$S \equiv Ls. \tag{2.1.7}$$

The examination of the actual influence of L is of interest in this context **[16-19]**. This can be achieved by simply increasing taper separation or by coating the end of the optical fiber with a highly reflective composite, which results in an interference length 2L

[16]. Increasing the distance L between the two tapers may actually increase the sensitivity of the sensor **[16, 17, 18]**.

One of the defining characteristics of a sensor based on a tapered optical fiber is the portion of light that is coupled out to the cladding, since, as has already been established, the effective RI of the cladding is more sensitive to changes in external parameters. One way of increasing the evanescent field is to create an offset: after the optical fiber is cleaved at a distance L from the first taper, a fusion splicing is performed with misaligned cores **[17]**. In fact, as either taper waist is decreased or core offset is increased, the attenuation increases, confirming that more light is lost to the surrounding environment. The sensitivity is increased when a more conventional interferometer with two short tapers in series is replaced by the configuration described before; the sensitivity is enhanced when L increases. Notably, for larger L, higher modes are efficiently excited in the cladding.

More exotic taper shapes were attempted in order to take advantage of a larger evanescent field **[25, 26]**.

Axial strain and RI were measured using a S-shaped taper **[25]**. The fabrication procedure relies on two main steps: cleaving the fiber and then splicing both ends with misaligned cores combined with tapering the region where the splice is. Different taper waists and axial offsets were tested; distinct sensitivities were reached: both RI and axial strain sensitivities tend to meet an enhancement when taper waist is decreased or when offset is increased (coupling efficiency is improved).

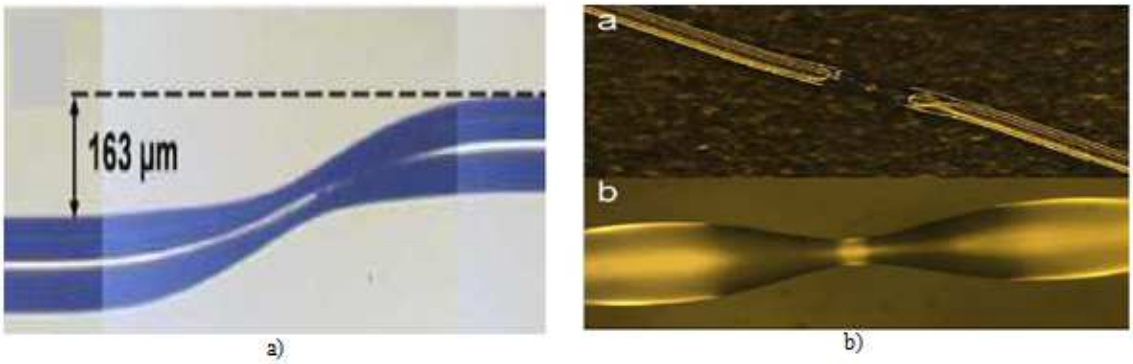

Figure 2.1.2 - a) S-shaped taper with an offset of 163 µm [25]; b) S-shaped taper for magnetic field [26].

Magnetic field sensing is also possible using an S-shaped taper **[26]**. This case is of interest since it stresses the wide range of applications for optical fiber sensors based on tapers. The external RI, in a fluid with magnetic nanoparticles, is linearly dependent on the applied magnetic field *H*, given the fact that the nanoparticles arrangement will be shaped by *H* (magnetic nanoparticle tend to form clusters along the direction H is applied). Knowing both the relations between RI and *H* (usually linear) and RI and wavelength shift, it is possible to monitor *H* by evaluating how the interference spectrum of the taper evolves.

Michelson interferometer-like sensors have also drawn attention **[27-31]**. The usual arrangement consists of a taper followed by a coated fiber end, which ensures light to be reflected and propagate back to the taper, as in a common Michelson interferometer **[27-29]**. A different configuration relies on a taper followed by a double-core fiber (DCF): the taper couples light, initially propagating along the core of a single-core fiber (SCF), into two cores. Then, light is reflected at the end of the DCF due to a coating applied to this interface. As the two separate beams approach the taper, they are coupled back into the SCF and forced to interfere. As in a Mach-Zender-like sensor, the principle of operation consists in monitoring the interference pattern as the external parameters change, more specifically, the evolution of the wavelength corresponding to a specific minimum of the pattern. This configuration renders the fiber intrinsically sensitive to bending **[30]**, since bending will create a difference in optical path between the two beams separated at the tapered region. A similar device can be used as a flow velocity sensor **[31]**.

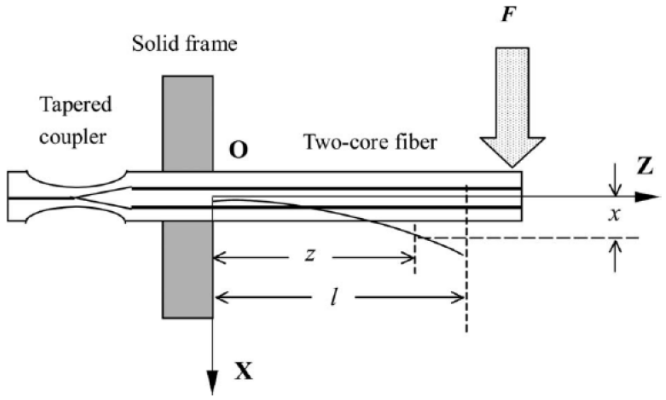

Figure 2.1.3 Michelson interferometer based on concatenated SCF and DCF via a taper for bending sensing [30].

A Fabry-Perot interferometer can also be implemented **[32]**. A taper is fabricated in the middle of a FBG, creating a structure that consists of two single FBGs with the same modulation period mediated by a long, very thin taper (microfiber), ending up resembling a cavity where radiation travels back and forth thanks to the successive reflections a given wavelength experiences when meeting the gratings. The sensor is based on the free spectral range (FSR) of the transmitted light dependence on the ambient RI.

Combining tapers and other structures like FBGs and LPGs has been considered **[33-37]**. RI measurement can be performed resorting to a fiber-tapered seeded LPG pair **[33]**. The Mach-Zender interferometer obtained with the LPG pair is improved by including a taper in-between both LPGs to enhance the sensitivity of the effective RI difference Δn_{eff}^{m} to the changes in external RI. An inclinometer based on a taper followed by an LPG was presented **[34]**. Once again, the presence of the taper enhances the coupling of light out of the core into the cladding, improving interferometer visibility. A larger sensitivity can also be achieved writing an FBG directly on a tapered region of the fiber when compared to that obtained in an untapered fiber.

Sub-wavelength taper waist diameters can turn out to be very appealing in novel, ground-breaking applications **[38, 45]**.

Even before the boom in optical fiber sensors took place, the notion that radiation pressure could be used to accelerate as well as trap particles was no stranger to the scientific community **[38, 39]**. A particle hit by a laser beam was drawn to the beam axis and accelerated in the direction of light. In a viscous medium, in the limit where the particle radius *r* is much smaller than the beam diameter w_0, the terminal velocity was found to be linearly dependent on laser power P and *r* , and inversely proportional to w_0 and viscosity of the medium η. The results were obtained considering a particle with characteristic dimensions close to the wavelength of the laser. Trapping using two laser beams with the same wavelength but propagating in opposite directions was also proposed. A single-beam trap mechanism was described **[39]**, reaching the Rayleigh particles with size as small as 25 nm (considerably smaller than the typical wavelength of a visible laser beam), which confirms a backward force component that helps holding the particle still in proximity of the optical fiber. The grounds for manipulation in the micro and nanometer scale were launched and optical tweezers have bloomed **[40, 41]**. These structures result from very thin tapers, able to create a dominant axial gradient force over scattering phenomena set in motion by radiation pressure, holding the particle near the optical tweezers. Holographic optical tweezers (HOTs) rest on the principle of optical trapping: placing a diffractive beamsplitter at the pupil's image converts a single input beam into several beams, each of which forms a separate optical trap. Such a beamsplitter can be a computer-generated hologram, and the resulting trapping patterns are known as HOTs.

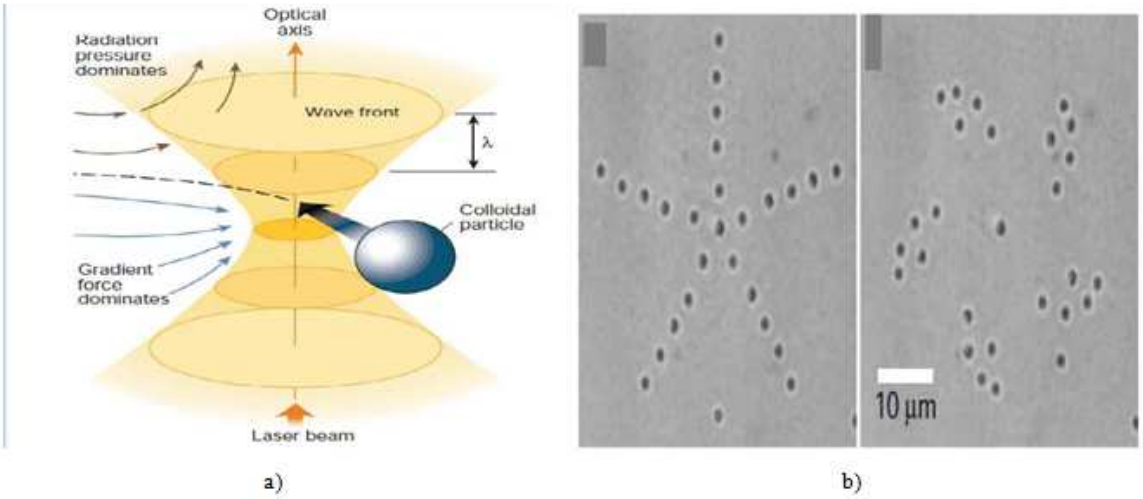

Figure 2.1.4 – a) Dominance of different phenomena (gradient force vs. radiation pressure) as the waveguide diameter varies; b) two different trapping pattterns making use of HOTs [40].

A detailed description of micro and nanofiber fabrication techniques and peculiarities can be found in the literature **[42]**. Some characteristics are highlighted: *strong confinement*, since the electric field is confined over a very small area over a significantly large distance (especially when both are compared) which explains why nonlinearities are easily observed in these fibers; *large evanescent fields*, as the thinned tapered region allows for a considerable portion of the field to propagate in the waveguide formed by the coating and the surrounding environment; *great configurability*, owing to the fact that optical fibers are somewhat mechanically forgiving and relatively small, being promptly integrated in complex configurations; *low-loss connections*, due to fiber diameters at input and output unchanged during the tapering process. The losses across the taper depend on the fabrication technique employed; two techniques were proposed: a flame-brushing technique and a modified flame-brushing technique, category into which CO_2 laser falls.

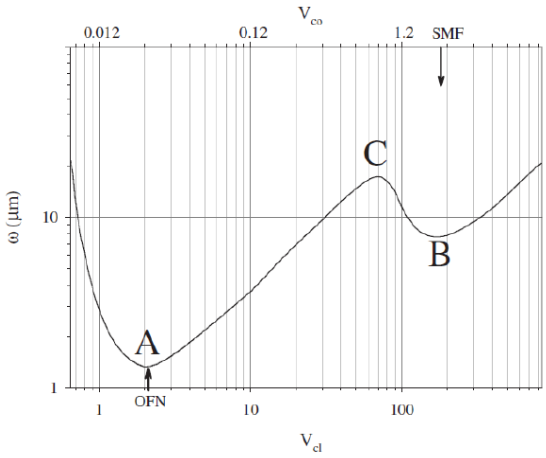

Figure 2.1.5 – Different regimes of light propagation as fiber diameter decreases ($\lambda = 1.55$ μm) [42].

Figure 2.1.5 helps understand the different regimes of light propagation that can be achieved when we move from a normal taper, to a slightly tapered fiber and then to a micro or nanofiber. As fiber diameter grows smaller, so do the *V* numbers concerning core, V_{co}, and cladding, V_{cl}. Before reaching B, the spot size of the beam ω decreases monotonically; the following growth in ω is explained by light propagating no longer solely along the core but also along the cladding. After the maximum C, ω decreases again; as V_{cl} approaches 2, the mode now propagates along the waveguide formed by the cladding and the surrounding environment, and ω grows again. This regime is typical for a nanofiber.

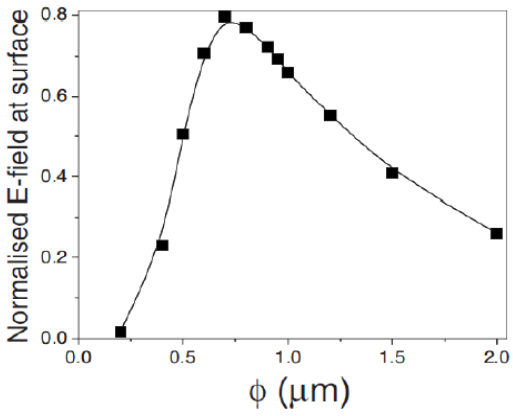

Figure 2.1.6 – Evanescent field at the fiber surface for several fiber diameters (λ = 1.047 μm and n = 1.45) [42].

As the fiber becomes thinner (right to left in Figure 2.1.6), two trends ought to be highlighted: the evanescent field increases, due to light no longer being confined to the core, spreading out more easily, then it decreases; this last observation is intriguing at first sight, but can be unraveled if particular attention is drawn to the fact that for diameters ϕ smaller than the maximizing $\phi = 0{,}75\mu m$ ($V_{cl} \sim 1$), the spot size ω is already considerably large which results in decreased power density. The small fiber diameter could suggest low mechanical strength, but, in fact, it can reach values higher than 10 GPa for smaller diameters.

Such promising results were put to good use in a variety of sensing schemes. One of the first consists of a hydrogen detector using nanofiber taper coated with palladium **[43]**. When the device is exposed to hydrogen, a change in the palladium layer is triggered, which, in turn, changes the evanescent field. The transmission becomes a function of the hydrogen concentration.

A nanoparticle detector is devised using a microfiber (with sub-wavelength waist diameter of approximately $0{,}8\ \mu m$) **[44]**. The evanescent field is perturbed by the presence of nanoparticles that bind to the surface of the taper. The power transmitted changes, presenting a characteristic time evolution that consists of several steps of given height. The presence of a step indicates that a particle has reached the taper surface; the height of the step is related to the size of the particle. The number of nanoparticles as well as their size can be determined.

Microresonators with two FBGs mediated by a portion of microfiber (Fabry-Perot-like device) can be characterized by a large Q-factor that renders them suitable for the study of nonlinear effects (usually associated to high radiation intensities). This kind of structure also allows for the observation of coherent cavity quantum electrodynamics (CQED), regime under which the interaction between light and matter is enhanced. These phenomena occur when the emitter-light coupling strength is much greater than the cavity photon decay rate and the free-space spontaneous emission rate of the emitter; such

conditions could be achieved resorting to a high finesse, low free spectral range device resembling the proposed Fabry-Perot cavity **[45].**

2.2 Analysis of the shape of a taper

The shape of a taper can be predicted through knowledge of the fabrication parameters, namely the variation of the *hot zone* (fiber length that is being actively transformed) **[14]**.

Assuming that during the fabrication of the taper there is no change in the volume of the fiber (the temperature reached is not high enough to cause significant evaporation of any of the fiber components) and that the fiber is cylindrical, then

$$V(r,L) = V(r+\delta r, L+\delta x) \Leftrightarrow \pi r^2 L = \pi (L+\delta x)(r+\delta r)^2 , \tag{2.2.1}$$

where L is the length of the *hot zone*, r is the radius of the fiber, δr and δx are the variations in radius and in the length of the *hot zone*, respectively. Casting Eq. (2.2.1) in a simpler form

$$\left(\frac{r}{r+\delta r}\right)^2 = \frac{(L+\delta x)}{L} . \tag{2.2.2}$$

considering δr much smaller than r,

$$\left(\frac{r}{r+\delta r}\right)^2 = \left(\frac{1}{1+\delta r / r}\right)^2 \approx 1 - 2\frac{\delta r}{r} . \tag{2.2.3}$$

Substituting (2.2.3) into (2.2.2), a very familiar and comforting-looking expression is obtained

$$\frac{dr}{dx} = -\frac{r}{2L} , \tag{2.2.4}$$

which agrees with the expected: as the *hot zone* increases, the radius decreases, hence the minus sign in Eq. (2.1.4).

Integrating both sides, after isolating each variable, yields

$$\int_{r_0}^{r} \frac{dr}{r} = -\frac{1}{2}\int_{0}^{x} \frac{dx}{L(x)}, \tag{2.2.5}$$

being r_0 the radius of the untampered fiber. Given that L is a function of the variation of the *hot zone* length that has gone unattended to so far in this discussion, only the left-hand side of Eq. (2.2.5) can be explicitly written, resulting in

$$r(x) = r_0 \exp\left(-\frac{1}{2}\int_{0}^{x} \frac{dx}{L(x)} \right). \tag{2.2.6}$$

An explicit expression for L has to be considered in order to carry on developing this model. A relatively simple formula for L as a function of x is critical in order to allow an easy implementation of this model. A linear relation sounds very appealing. For $L(x) = L_0 + \alpha x$, where L_0 is the initial length of the *hot zone* and α is the rate of taper elongation,

$$r(x) = r_0 \exp\left(-\frac{1}{2}\int_{0}^{x} \frac{dx}{L(x)} \right) = r_0 \left[1 + \frac{\alpha x}{L_0} \right]^{-\frac{1}{2\alpha}}. \tag{2.2.7}$$

The expression for r as a function of x is useful for the fabrication procedure. However, to trace the profile of the taper, finding an expression for r as a function of the position z along the fiber is required. z can be related to x and L by the distance law

$$2z = x + L_0 - L = x(1+\alpha). \tag{2.2.8}$$

Substitution in Eq. (2.2.7) readily gives

$$r(z) = r_0\left[1+\frac{2\alpha z}{(1-\alpha)}L_0\right]^{-\frac{1}{2\alpha}}. \qquad (2.2.9)$$

Some attempts to implement this method have been performed resorting to a CO_2 laser **[15]**. The outcome of those attempts shows that a fairly good agreement between theoretical predictions and experiment can be met.

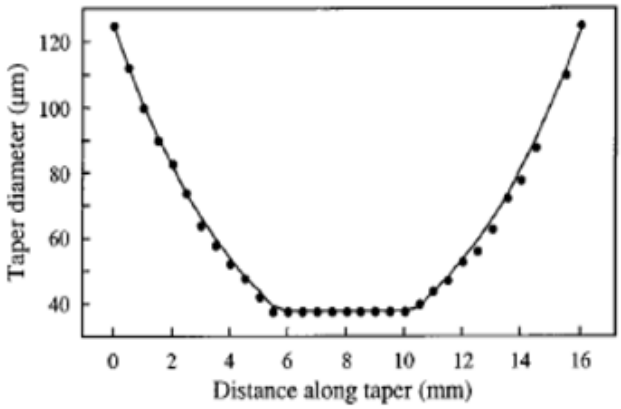

Figure 2.2.1 – Exponential profile obtained for a constant hot zone (α = 0). Theoretical prediction (solid line) and experimental results (circles) are depicted [15].

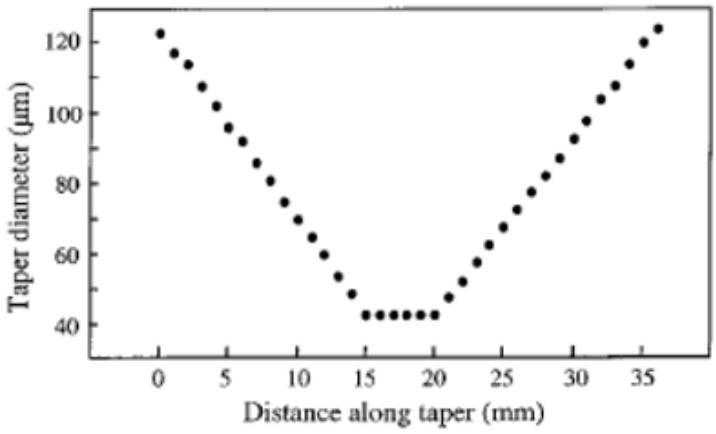

Figure 2.2.2 – Linear profile obtained for α = -0.5 [15].

Besides the shapes associated to $\alpha = 0$ and $\alpha = -0.5$, other cases are worth mentioning like the profile for α very close to one, which can be described as a very abrupt transition between the untapered and the tapered regions; for an adiabatic taper, the transition region should be long, presenting a smooth decreasing profile for $r(z)$. The adiabaticity condition is given by

$$\left|\frac{dr}{dz}\right| \leq \frac{r(\beta_1 - \beta_2)}{2\pi}, \tag{2.2.10}$$

where β_1 and β_2 are the propagation constants for the fundamental and the higher order modes between which energy exchange occurs. Handling this expression is a challenging and somewhat tricky endeavor, since β_1 and β_2 are functions of r. A strategy can be devised to get rid of the inequality, resorting to a constant f that evaluates how smaller $\left|\frac{dr}{dz}\right|$ is when compared to $\frac{r(\beta_1 - \beta_2)}{2\pi}$. Since $r(z)$ is a decreasing function , the left-hand side of Eq. (2.2.10) is negative. Combining all the previous considerations, an implicit solution is found

$$z(r) = \frac{2\pi}{f}\int_{r_0}^{r} \frac{dr}{r[\beta_2(r) - \beta_1(r)]}. \tag{2.2.11}$$

The job is still unfinished as the propagation constants need to be numerically computed. Further details can be found elsewhere **[32, 46, 47]**. The fabrication should rely on a choice of α close to zero and a large L_0, in order to reproduce an approximately exponential, slowly decreasing profile.

2.3 CO_2 laser interaction with an optical fiber

A CO_2 laser is characterized by high power and efficiency **[48]**. Light emission takes place between two vibrational levels of the CO_2 molecule with an energy gap corresponding to a 10.6 μm wavelength. Adding to this the fact that light absorption by silica-based glasses, which are the main components of optical fibers, is strong near this wavelength, CO_2 lasers are undeniably appealing when it comes to the possibility of shaping an optical fiber, for instance by reducing its diameter to sub-micrometer values, or the possibility of creating structures based on refractive index modulation. Such modulation and reconfiguration of the fiber shape can be achieved by simply heating the fiber **[49-54]**.

An estimate of the magnitude of the refractive index change that can be obtained shining light provided by a CO_2 laser on a fiber is given by **[49]**

$$\Delta n = -6.35\times10^{-6}\sigma \tag{2.3.1}$$

where σ is the total residual stress in the fiber as a result of heating. The contributions to σ can be separated in thermal (σ_{th}) and elastic ($\sigma_{el,co}$ for the core and $\sigma_{el,cl}$ for the cladding) residual stresses. Eq. (2.3.1) emphasizes the direct contribution of stress to the refractive index change. After the fiber is heated up by the CO_2 laser radiation, some frozen stress and strain are left even though no external force is applied, which can be a result of different thermal expansion coefficients or viscosities of the core and cladding; they can also be explained by changes in material structure **[55, 56]**. These frozen stress and strain do change the refractive index of the fiber. Thermal residual stress can be computed, knowing how temperature changes along the radial direction of the fiber. A rather complete and elucidating treatment can be found, concerning the expressions for the spatial dependence of temperature as well as for σ_{th} , $\sigma_{el,co}$, $\sigma_{el,cl}$ **[49, 56]**. The analysis of the final results should suffice in order to comprehend the implications of the interaction under scrutiny.

The time evolution of the temperature T is of interest, showing a fast growth in the first seconds followed by a regime of quasi-constant temperature as saturation is approached. In this limit **[57]**,

$$\Delta T(0,0,t) = \frac{Ia}{\sqrt{\pi}k_e}\tan^{-1}\left(\sqrt{\frac{4D_e t}{a^2}}\right), \tag{2.3.1}$$

where $\Delta T(r=0,z=0,t)$ is the temperature variation, at a given time t, in the spot where the radiation hits the fiber ($r=0$ indicates the surface and $z=0$ indicates no axial translation), I is laser intensity, a is the $1/e$ radius of the beam, k_e is the thermal conductivity and D_e is the thermal diffusivity; these last two parameters can be considered to be approximately constant in the range of temperatures considered (up to 2500K). The saturation can be found making $t \to \infty$,

$$\Delta T_{sat} = \frac{Ia}{\sqrt{\pi}k_e}\lim_{t\to\infty}\tan^{-1}\left(\sqrt{\frac{4D_e t}{a^2}}\right) = \frac{Ia}{\sqrt{\pi}k_e}\frac{\pi}{2} = \frac{Ia\sqrt{\pi}}{2k_e}. \tag{2.3.2}$$

The saturation value is expected to increase when both laser power and beam radius increase. Figure 2.3.2 also emphasizes the fact that temperature starts to increase sooner for higher power. Temperature increases faster for the front surface of the cladding (directly shone upon by the laser light) than it does for the core; the back surface meets the slowest increase of all.

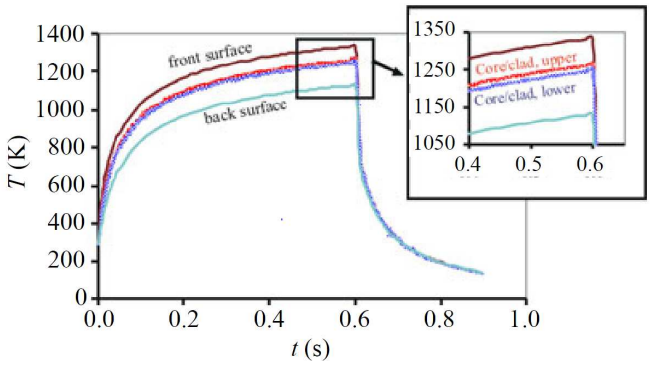

Figure 2.3.1 – Time evolution of the temperature for the cladding (front and back surfaces) and core. Inset: detail of the core-cladding interface. The laser delivered a power of 6 W for 0.6 s and the data are collected at the point where the light hits the fiber (ellipsoidal shape for the beam with $\boldsymbol{r_x = 0.15\ mm}$ and $\boldsymbol{r_y = 1.75\ mm}$) [49].

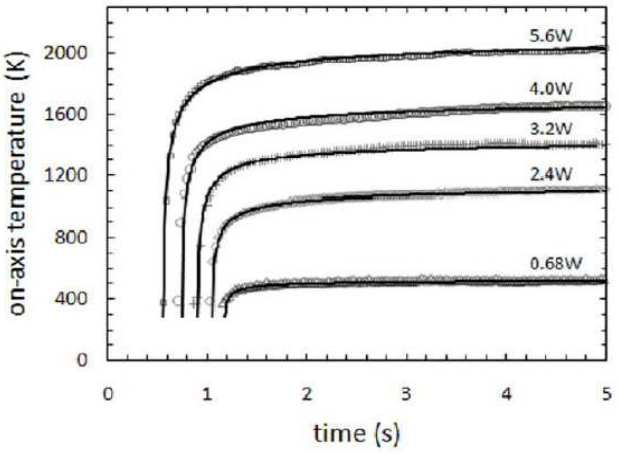

Figure 2.3.2 – Time evolution of the temperature of the front surface as laser power is increased (1 mm beam diameter). Solid line corresponds to manufacturer´s data [57].

The spatial profile of the temperature is obtained for the cladding (front and back surfaces) and for the core **[49]**. The profile is Gaussian for all the portions of the fiber under analysis, as expected taking into account the spatial dependence of the intensity delivered by the laser, which means the effect of heating a portion of the fiber spreads out to a distance that is related to the diameter of the beam. The maximum temperature registered decreases the farthest the part of the fiber being studied is from the point where radiation hits it (along the radial direction). The spatial dependence is also depicted for different time instants and laser powers **[57]**. The maximum temperature and broadness of the curve increase as time grows longer and laser power grows larger.

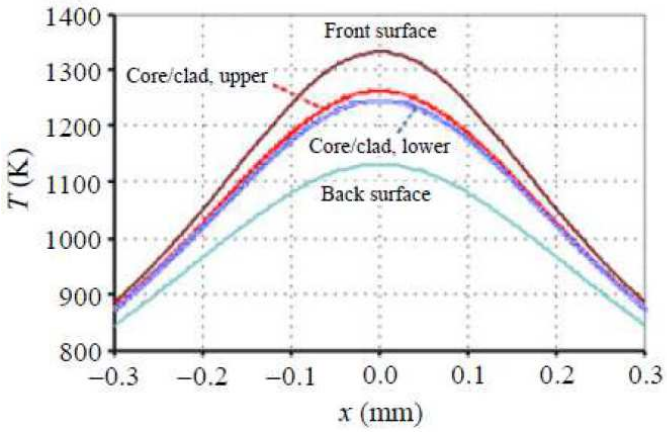

Figure 2.3.3 – Temperature spatial profile along the axial direction of the fiber. The laser delivered a power of 6 W for $\mathbf{0.6\ s}$ (ellipsoidal shape for the beam with $\boldsymbol{r_x = 0.15\ mm}$ and $\boldsymbol{r_y = 1.75\ mm}$) [49].

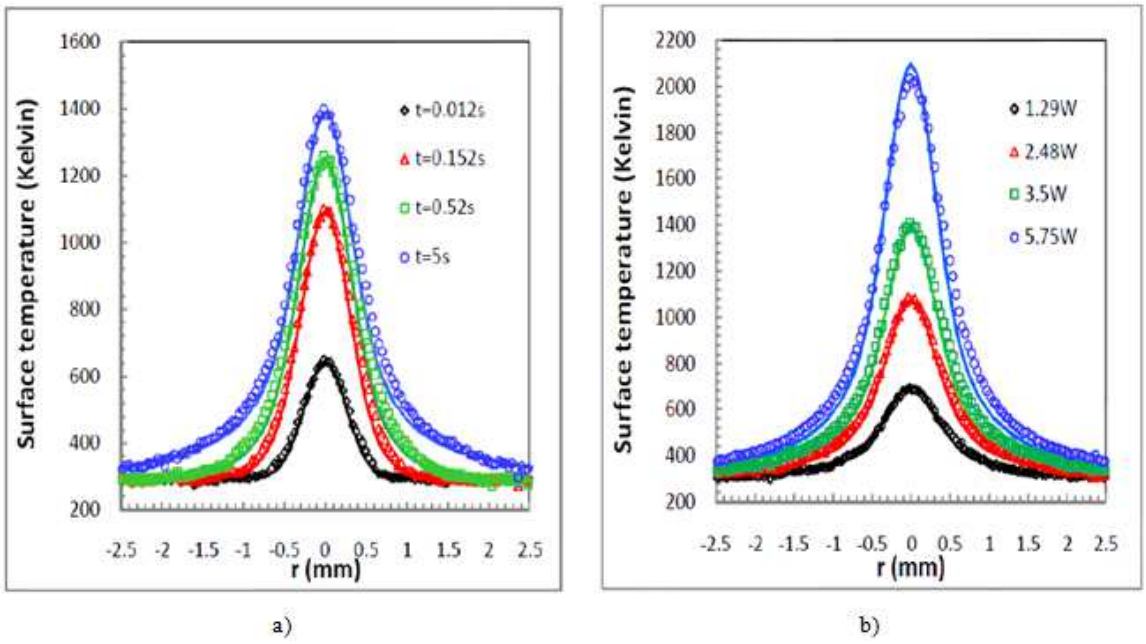

Figure 2.3.4 – Temperature spatial profile along the axial direction of the fiber for a) different time instants (3.5 W) and b) different laser powers (steady-state) (1mm beam diameter for a) and b)) [57].

A surprising outcome emerges from evaluating how the refractive index is influenced by the previously studied temperature behaviors: the main changes occur in the cladding, both in the front and back surfaces, even though the temperature is higher for the core (when compared to the back surface); such observation goes to show that this kind of modulation not only depends on the temperature reached but also on the material whose

refractive index is being modified. This result may suggest that the modulation is mostly achieved by changing the refractive index of the cladding, whereas the core undergoes a fainter increase. In fact, even though the core refractive index experiences a smaller variation, it contributes significantly to the overall modulation. This idea is corroborated by investigating what happens to excited asymmetrical higher-order modes in the cladding in the context of a LPG structure **[54]**. The refractive index modulation asymmetry depends on both laser power, irradiance time elapsed and beam diameter: for larger diameters and longer irradiance times, a more pronounced asymmetry is obtained. The resulting asymmetrical modes can be almost entirely wiped out if the cladding radius is significantly reduced by etching, while symmetric modes persist. The asymmetrical traits of refractive index modulation are mainly connected to modulation in the cladding. Despite the smaller change in refractive index, the core also plays an important role in this modulation, especially when it comes to its symmetrical characteristics.

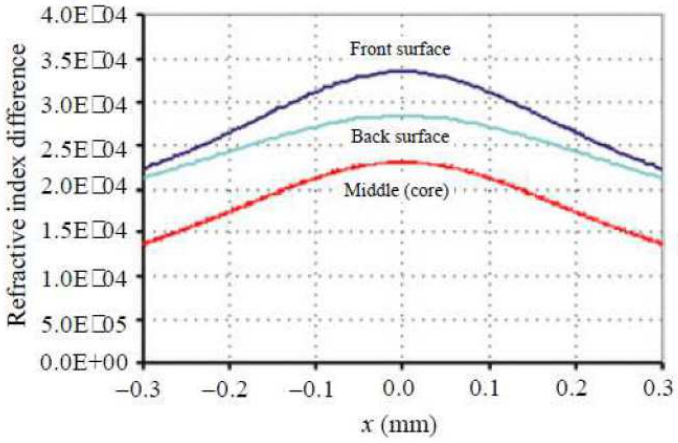

Figure 2.3.5 – Refractive index change in the cladding (front and back surfaces) and in the core after delivering 6 W for 0.6 s (ellipsoidal shape for the beam with $\boldsymbol{r_x = 0.15\ mm}$ and $\boldsymbol{r_y = 1.75\ mm}$) [49].

The peak refractive index changes are 3.4×10^{-4} in the cladding and 2.3×10^{-4} in the core **[49]**. Similar values can be found in other attempts to modulate the refractive index of an optical fiber core and cladding resorting to a CO_2 laser **[54]**.

By heating an optical fiber with a high power CO_2 laser, its refractive index can be changed by an order of magnitude of approximately 10^{-4}, rolling out the red carpet for the

fabrication of structures like LPGs. If the achieved temperatures are near the melting point of silica (~ 2000K) and axial tension is added in the mixture, in order to stretch the fiber, tapers can also be produced.

3. Taper fabrication I – applied mechanical stress through attached weights

3.1 Experimental Setup

The experimental setup devised for taper fabrication relies on a SYNRAD 48-1 CO_2 laser providing infra-red (IR) radiation with 10.6 μm wavelength and 10 W maximum output power, high enough to reach the melting point of silica (~ 1700 ℃). A crude estimate considering a power of 2 W, a 2 mm beam diameter and an emissivity of 0.9 (typical of glass and reasonably applied to a silica-based material such as our optical fiber), yields a temperature of approximately 1600 ℃. The high-power radiation delivered onto the optical fiber is then responsible for a significant increase in its temperature, rendering the fiber more ductile and making it possible to locally change its shape. For this method to work, a weight attached to the fiber is required to place it under more mechanical stress (in addition to that resulting from heating). The use of weights with different masses is expected to result in different taper shapes (length, thickness) and, consequently, have a considerable impact on the characteristics of the transmitted light. Beam manipulation is performed resorting to two protected silver mirrors with 25.4 mm diameter, a ZnSe coated plano convex lens with 25.4 mm diameter and 100 mm focal length and a silver protected concave mirror with 50.8 mm and 150 mm focal length. The first mirror reflects the beam at 45º allowing it to reach the height of the stages; the second mirror also reflects the light at 45º directing it towards the ZnSe coated lens. The lens is mounted on a manually controlled stage which allows for lens-fiber distance to be changed, resulting in different beam diameters when the latter hits the fiber; the concave mirror collects radiation that was not trapped in the fiber, sending it back and minimizing power losses and contributing to a more symmetrical taper shape. The importance of the concave mirror is emphasized if an estimate of the beam diameter at the focal plane is performed, resulting in a value close to 400 μm, considerably larger than the fiber diameter (~ 125 μm), meaning a complete superposition of the beam onto the fiber is not achieved.

Taper quality evaluation consists of analyzing its shape and transmission spectrum. The shape evaluation is conducted using a BRESER USB microscope with a digital camera and the evaluation of the transmission spectrum is performed using a YOKOGAWA

AQ6370C Optical Spectrum Analyzer (OSA) which receives light, provided by a broad-band light source (central wavelength 1550 nm with a bandwidth of 100 nm and an average power of -30 dBm), that travels through the fiber and the taper.

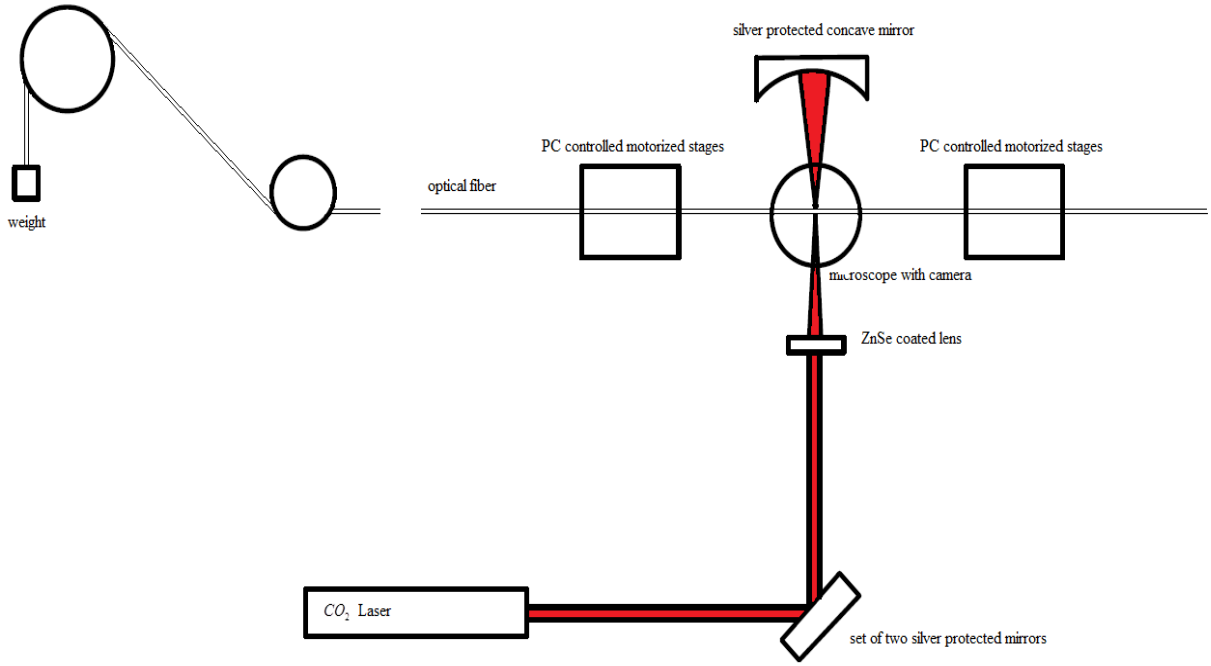

Figure 3.1.1 – Experimental setup for taper fabrication using a $\mathbf{CO_2}$ laser.

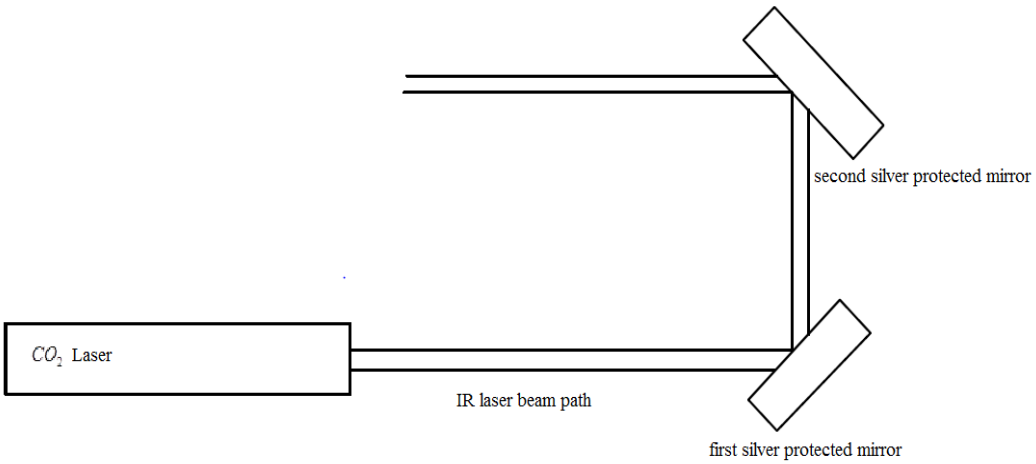

Figure 3.1.2 – Lateral view of the experimental setup (in order to have the laser beam path exactly depicted, the second mirror would have to be rotated 90º into the paper, redirecting the beam along the same direction).

Some of the CO_2 laser output beam characteristics, such as power (P), can be controlled by a remote control activated manually or automatically. In either case, it is possible to set the pulse width modulation PWM as well as the frequency of the pulse responsible for exciting the CO_2 active medium (set equal to 5 kHz). The laser output power is changed by varying the PWM: the establishment of a relation between power and PWM is of the essence.

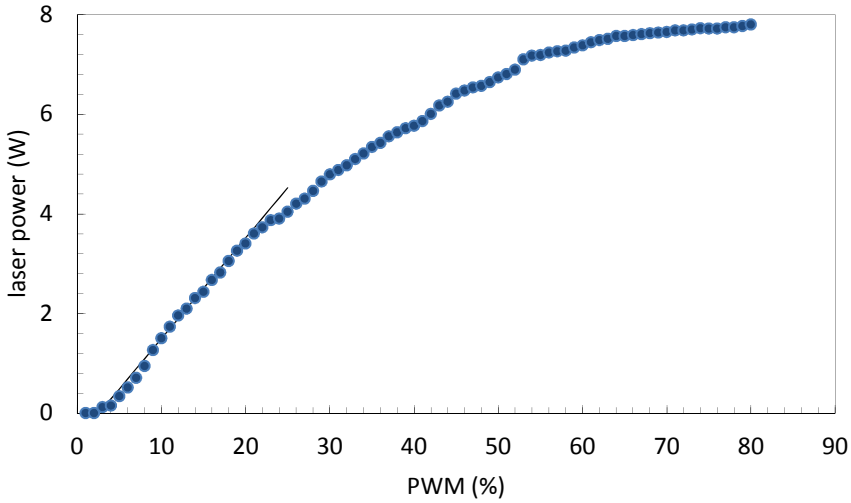

Figure 3.1.3 – Power vs. PWM. Line (linear fit).

The graph reveals an approximately linear behavior for low PWM; considering values up to 25%, an approximate expression for the dependence of power P on the PWM can be written as

$$P \approx (0.202 \times PWM - 0.52)\,. \tag{3.1.1}$$

One should be careful not to apply this expression to values of PWM below a certain limit, since the power obtained would be negative. PWM should then be larger than 2.6 % for the expression (3.1.1) to be valid. As higher values for the pulse width are considered, a saturation regime is reached. The average of the registered power oscillations is under 6 %. The measurements were performed using a COHERENT LM45 FieldMaster power detector with a 10 W damage threshold.

3.2 Analysis of the experimental results

The analysis of the experimental results obtained, as taper fabrication is attempted using small weights attached to the fiber to provide mechanical stress, focuses essentially on the time evolution of two taper characteristics: length and transmission spectrum.

As far as the time evolution of the taper length is concerned, a general trend is verified: as time goes by, the length of the taper increases; as the end of the fabrication process approaches, the rate of growth becomes larger. Resorting to weights with different masses (m), which means resorting to different applied mechanical stresses, the profiles of the best-fit curves change, since for larger masses the process occurs in a quicker fashion and the final increase in the growth rate appears to be more significant. The best-fit curves are both polynomial.

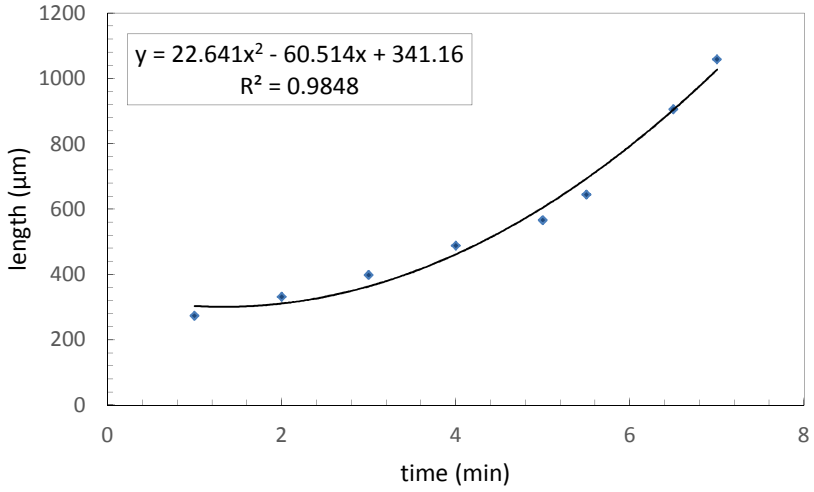

Figure 3.2.1 - Taper length time evolution (P = 1.5 W; m = 3 g); experimental data and best-fit curves are depicted.

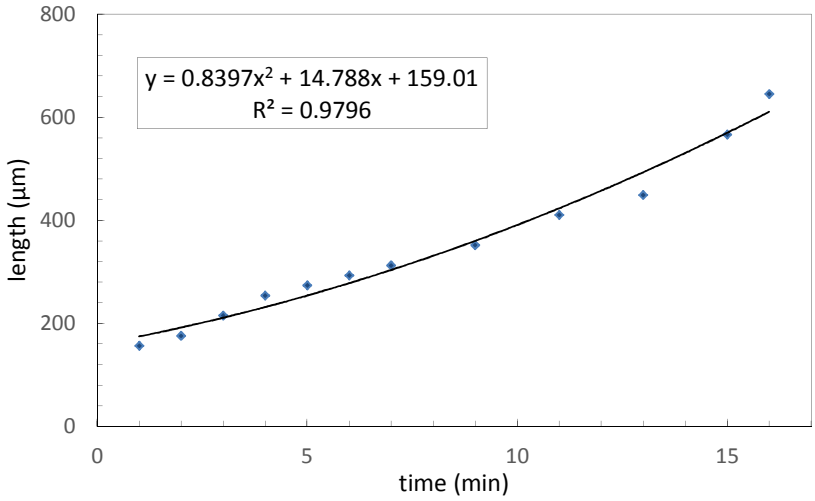

Figure 3.2.2 - Taper length time evolution (P = 1.5 W; m = 2 g); experimental data and best-fit curves are depicted.

The time evolution of the transmission spectra reveals a decrease in the average power. This behavior is expected taking into account the previous knowledge concerning the basic principle of operation of a taper both as a coupler or a sensor: light has to couple out of the core into the cladding; some of the power associated to the light traveling along the cladding is bound to be transmitted to the surrounding environment of the fiber, contributing to the previously mentioned decrease in the average power. Despite the approximately steady and predictable evolution of these spectra throughout most of the process, a peculiarity that sometimes takes place in the beginning of the fabrication should be mentioned. As the radiation hits the fiber, an abrupt decrease in the average power is verified, followed by a relatively quick return to values close to those that characterize the source. This event can be explained by the sudden increase in temperature experienced by the fiber that leads to a local change in refractive index as well as to a considerable modification of the fiber profile.

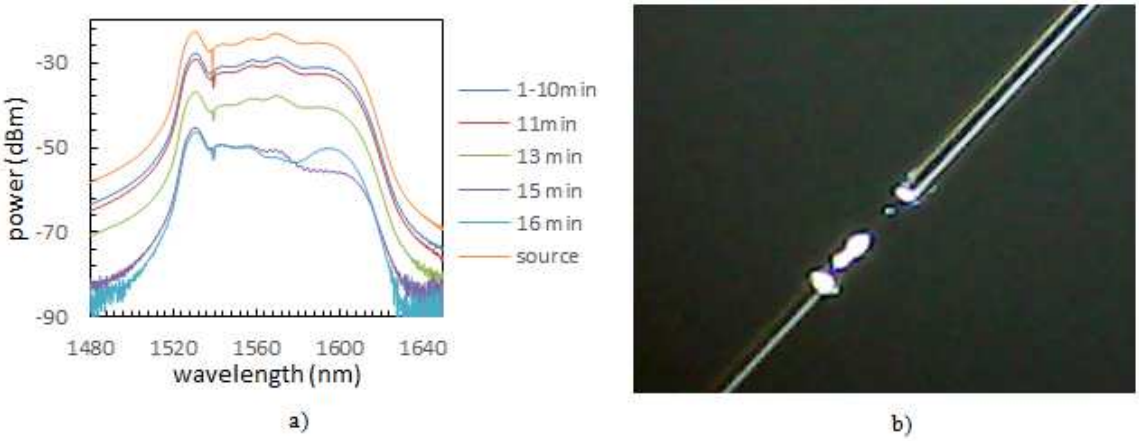

Figure 3.2.3 – a) Transmission spectrum time evolution; b) Taper for t = 16 min, with 645 μm; (P = 1.5 W and m = 2 g).

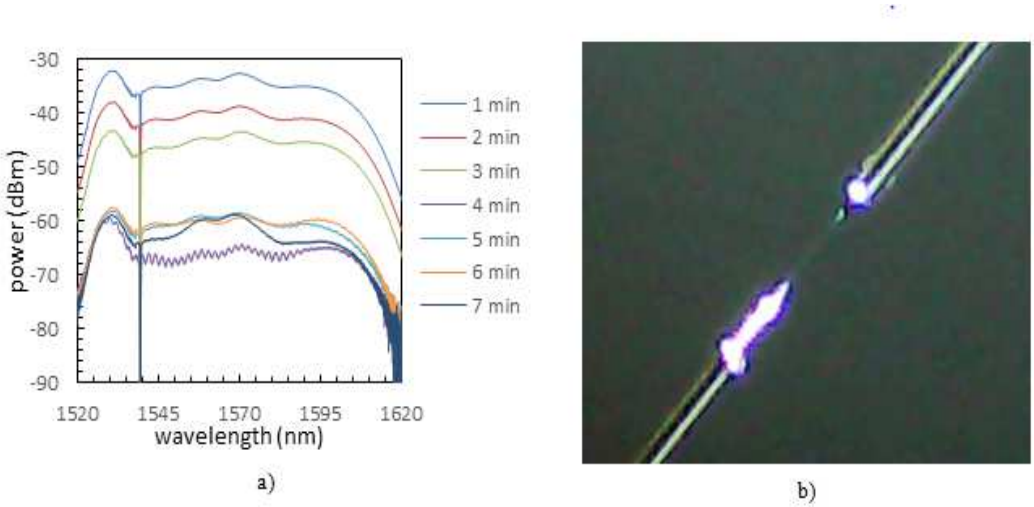

Figure 3.2.4 - Transmission spectrum time evolution; b) Taper for t = 7 min, with 1058 μm; (P = 1.5 W and m = 3 g).

Another important aspect is linked to the fact that, as the taper waist diameter grows narrower, the available bandwidth decreases. One might also notice that a Fabry-Perot-like interference pattern creeps in at certain stages of the fabrication process (at 15 min and at 4 min in the graphs in Figure 3.2.3 and in Figure 3.2.4, respectively). A Fabry-Perot cavity consists of two mirrors with reflectivities R_1 and R_2 between which there is a medium with refractive index n_2. This kind of cavity resembles approximately the structure created while fabricating a taper: the refractive index change along the length of the taper results in

two interfaces between media with different refractive indices (n_2 inside the confinements of the taper and n_1 for the unchanged fiber) that can act as two mirrors. As a consequence, part of the light will travel back and forth inside the taper giving rise to the introduction of interference fringes typical of this kind of interferometer. The fact that these fringes only show up momentarily can be understood by studying the dependence of the Fabry-Perot transmitted power T_{FP} on the reflectivities and on the angle of incidence of light upon the two interfaces θ (which constitutes an obvious simplification in this case, since the angle of incidence is not necessarily the same for both interfaces), expressed as **[48]**

$$T_{FP} = \frac{T_1 T_2}{\left[1-(R_1 R_2)^{1/2}\right]^2 + 4(R_1 R_2)^{1/2}\sin^2(\phi)}, \tag{3.2.1}$$

where ϕ is a function of θ; T_1 and T_2 can be written as $T_n = 1 - R_n - A_n$, where A_n characterizes the losses at a given interface (due to absorption). The appearance of these interference fringes can be seen as the result of a combination of values for R_1, R_2 and ϕ that leads to a significant increase for T_{FP}. Said combination can be reached when θ is such that $\sin^2(\phi) \approx 0$ and when R_1 and R_2 are very close to each other. Since the process under analysis is characterized by variations in the refractive index (therefore in the reflectivities of the interfaces at both ends of the taper) as well as in the shape of the taper (resulting in different θ), the obtained Fabry-Perot interference pattern can be considered rather unstable, which explains its relatively quick disappearance.

The analysis of the taper shape reveals a clear longitudinal asymmetry (along the direction of light propagation in the fiber). This is a consequence of having the laser radiation always hitting the fiber at the same spot, creating one end of the taper with much smaller diameter than the other. The resulting abrupt transition near this end can be responsible for a great deal of power loss.

Attention should be drawn to the fact that the reproducibility obtained using the proposed experimental setup and procedure is not assured: the data in the graphs in Figures 3.2.3 and 3.2.4 show that, despite approximate experimental conditions (power and weight

mass), the time elapsed to obtain tapers roughly the same size is substantially different (from 16 min for the first taper to 7 min for the second one). This has to do with extra degrees of freedom in the procedure associated with the superposition of the laser beam over the fiber and the kind of mechanical stress that results from attaching the weights to the fiber: despite always trying to have the best superposition and always striving to attach the weights the same way, such efforts are not enough to avoid some unwelcome disparities like the significantly different times elapsed during the fabrication.

For thinner tapers, the transmission spectra show a very promising profile with interference fringes.

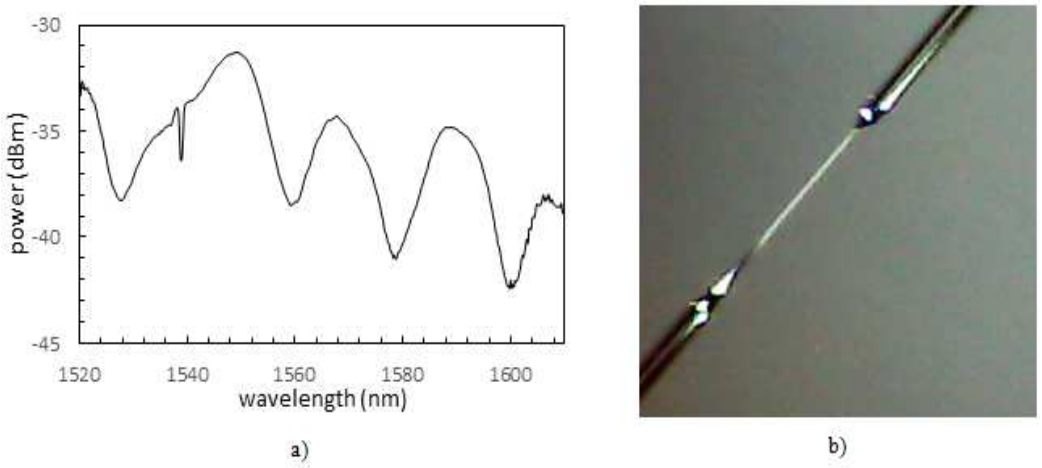

Figure 3.2.5 – a) Transmission spectrum for a thin taper; b) Thin taper, with 1100 μm; (P = 1.5 W and m = 4 g) .

Once arrived at a stage in which effective interference between light travelling through the core and light travelling through the cladding takes place, the study of the time evolution of the transmission spectra grows in complexity and in relevance to the evaluation of the taper potential as a sensor.

The approach to the fabrication strategy was slightly different in this case, since the power was not the same during the entire process: for the taper under analysis, 22 min at a power of 1.5 W, until the point when fringes start to appear, and then reduced to 1.4 W in

order to be able to more closely and effectively accompany the evolution of the obtained spectra.

Up until 12 minutes after the appearance of the interference pattern, the evolution of the fringes does not seem to follow a discernible pattern, although, for each frozen time instant, there are clear interference patterns.

A very fulfilling result was obtained short past 12 min after the fringes first appear: the interference pattern preserves more or less its shape, apart from a continuous shift of its minima and maxima towards shorter wavelengths.

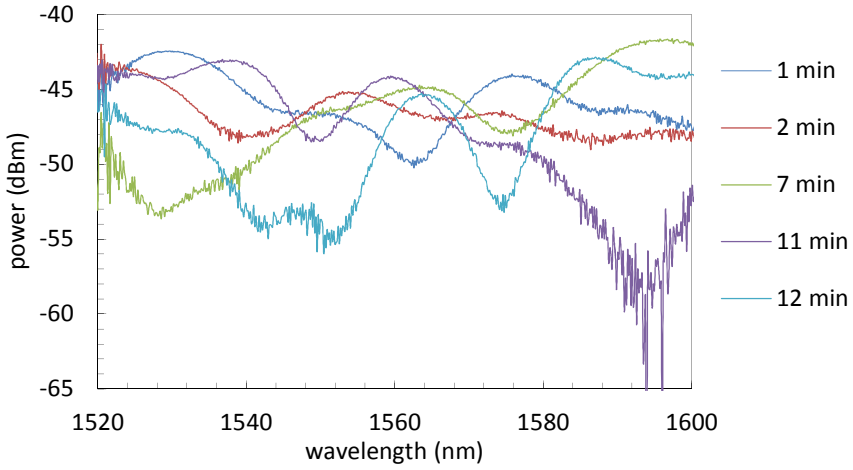

Figure 3.2.6 – Transmission spectrum time evolution (the time instants correspond to time after the fringes first appear).

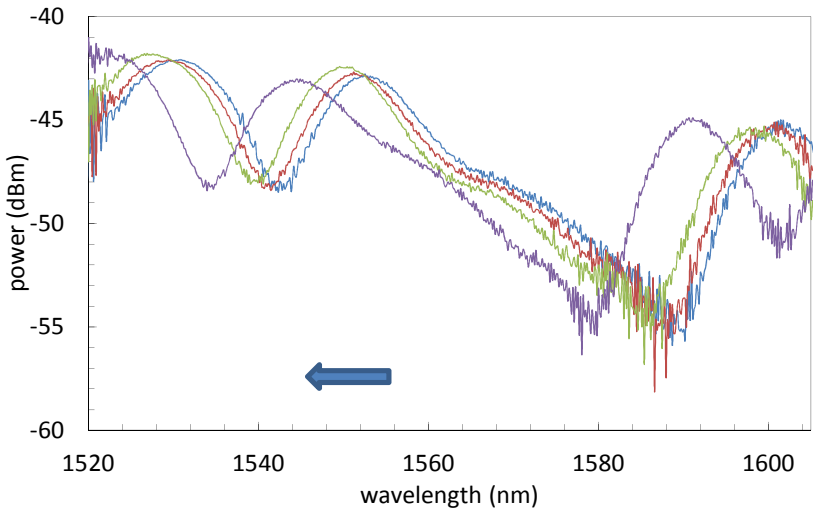

Figure 3.2.7– Transmission spectrum time evolution 12 min after the fringes first appear. The arrow sets the trend to the evolution as time goes by.

This more stable interference pattern confirms the anticipated potentialities of the tapers fabricated using a CO_2 laser as sensors, since the shift towards shorter wavelengths can be regarded as a consequence of the variation of external parameters. At this point, an attempt to characterize the taper as a sensor of temperature, refractive index or strain based on the results summarized in the graph of Figure 3.1.10 is futile, since the taper experiences a simultaneous change in many external parameters: the radiation produced by the CO_2 laser boosts the temperature of the fiber up to values close to the melting point of silica, variation in temperature which is accompanied by a change in refractive index as well as by the introduction of more mechanical stress due to, for example, different thermal expansion coefficients for the core and cladding. Despite this, promising results are verified, namely an approximately linear behavior characterizing the evolution of the minimizing wavelengths and the different slopes obtained for the two analyzed minima, at $\lambda_1 = 1542.35\,\text{nm}$ and $\lambda_2 = 1588.70\,\text{nm}$. The fact that an exact relation between time and the variation of the external parameters cannot be properly established should not discourage the excitement that comes from looking at the results in Figures 3.2.7 to 3.2.9, since, if said variation is not significantly large, then a linear relation between that variation and time can always be considered (through a Taylor series expansion), which leads to the highly

anticipated linear behavior for the wavelength shift as a function of the variation of the external parameters.

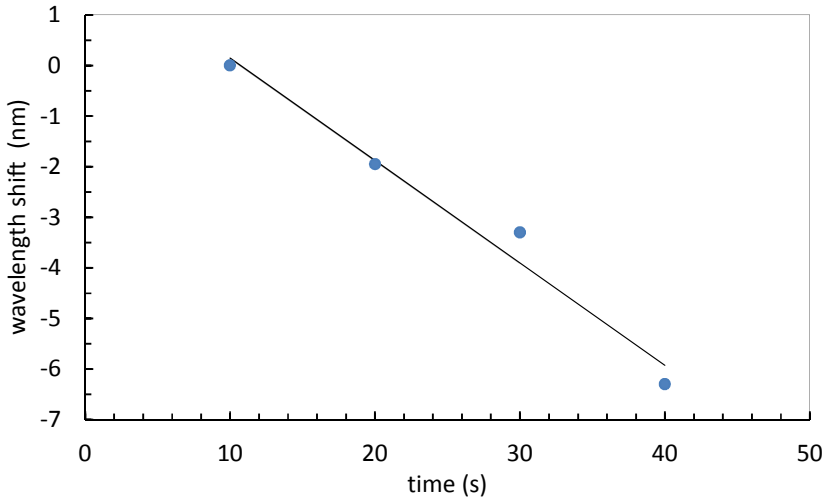

Figure 3.2.8 – Wavelength shift time evolution for λ_1=1542.35 nm. Line (linear fit).

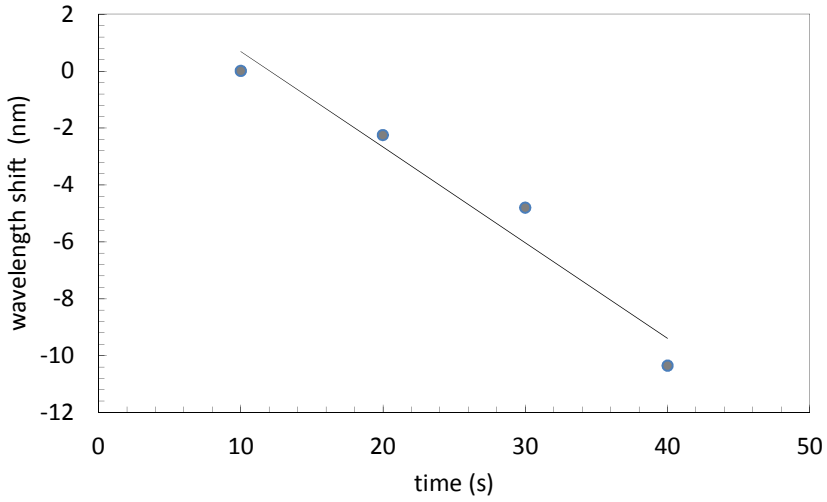

Figure 3.2.9 – Wavelength shift time evolution for λ_2=1588.70 nm. Line (linear fit).

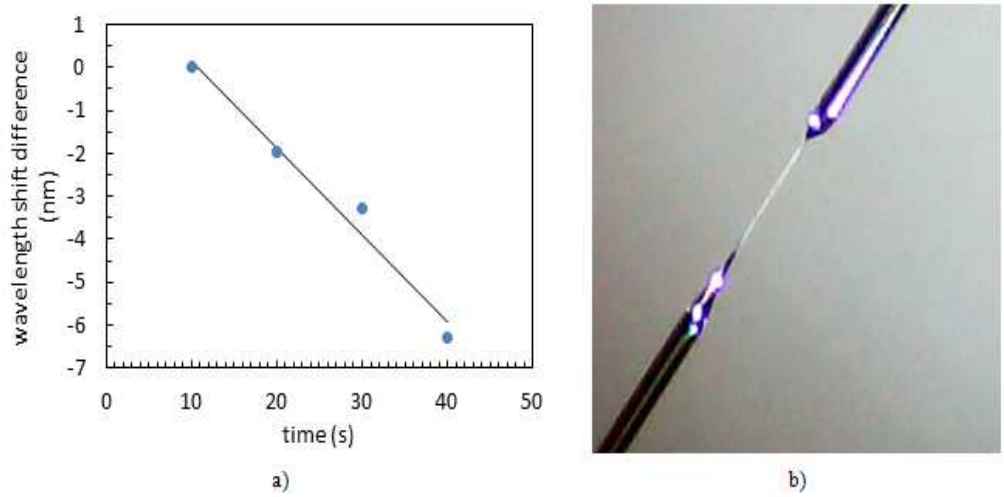

Figure 3.2.10 – a) Time evolution of the wavelength shift difference between minima at $\boldsymbol{\lambda_1 = 1542.35\ nm}$ and $\boldsymbol{\lambda_2 = 1577.70\ nm}$. Line (linear fit). b) Thin taper, with 860 μm; (P = 1.5 W for 22 min and then P = 1.4 W for 12 min; m = **2 g**).

The graph in Figure 3.2.10 a) clearly helps realize that, although the shift for the two minima considered presents an approximately linear relation with time, the slope associated to each one is different. This means that the sensitivity towards the change of a given external parameter is distinct for the two minima. If one wishes to effectively implement a taper as a sensor of a given external parameter, exclusively, then the influence of all the others should be accounted for. For this discrimination of physical parameters to be possible, then the sensitivity of different minima should, in fact, be different. Considering only as significant the variations in temperature ΔT and the variations in strain $\Delta\xi$, then the wavelength shifts for two different peaks $\Delta\lambda_1$ and $\Delta\lambda_2$ can be written, resorting to a linear approximation, as

$$\begin{cases} \Delta\lambda_1 = a\Delta T + b\Delta\xi \\ \Delta\lambda_2 = c\Delta T + d\Delta\xi \end{cases}, \tag{3.2.1}$$

where a, b, c and d stand for the sensitivities of each peak towards temperature and strain variations. The set of equations (3.1.2.) can be written using matrices as

$$\begin{pmatrix} \Delta\lambda_1 \\ \Delta\lambda_2 \end{pmatrix} = \begin{pmatrix} a & b \\ c & d \end{pmatrix} \begin{pmatrix} \Delta T \\ \Delta\xi \end{pmatrix} = S \begin{pmatrix} \Delta T \\ \Delta\xi \end{pmatrix}, \tag{3.2.2}$$

which only has a non-trivial solution if the determinant of the sensitivity matrix S is non-zero. Such condition implies that

$$ad \neq bc\,. \tag{3.2.3}$$

If the sensitivities of the chosen minima are the same, then the condition established by the inequality (3.2.3) is not verified. Therefore, in order to be able to discriminate between the influences of different physical parameters, one should have access to minima in the interference pattern with different sensitivities, which seems to be the case of the taper in Figure 3.2.10 b).

So far, the focus of this analysis has been directed towards the transmitted light. It can be interesting to check what happens to the light that is reflected by the taper. How much does it account for the power losses? Does the reflected light spectrum also present interference fringes? How does the average power evolve in time and how is it related to the decrease in the average power of the transmitted light?

The time evolution of the average power shows that, initially, the amount of light reflected by the taper is relatively small resulting in values for power very close to the noise level. As time goes by, this average power increases showing that the light spectrum approximately resembles the shape of that of the source, without ever approaching the typical shape of an interference spectrum.

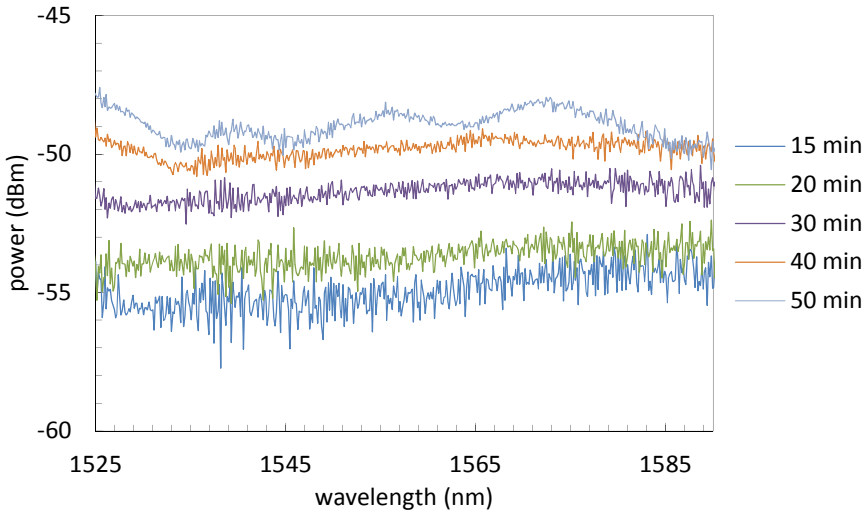

Figure 3.2.11 – Reflection spectrum time evolution.

This resemblance might lead to the conclusion that the light is mostly reflected at the extremity of the taper closest to the source, without any major contribution from the interface at the other extremity. The amount of light reflected can be boosted by the abrupt transition (point A in Figure 3.2.14) that can be found near the first extremity light reaches when travelling through the fiber. The increase in the average power can also be understood if one thinks, for example, of Fresnel equation for reflectivity at an interface between media with refractive indices n_1 and n_2, which results in a refractive index difference $\Delta n = (n_1 - n_2)$ **[59]**,

$$R = \left| \frac{n_1 \cos(\theta_i) - n_2 \cos(\theta_t)}{n_1 \cos(\theta_i) + n_2 \cos(\theta_t)} \right|^2 . \tag{3.2.4}$$

For the case under consideration, n_1 corresponds to the refractive index of the fiber outside the confinements of the taper, approximately constant, and n_2 to the changing refractive index of the fiber inside the confinements of the taper. Bearing in mind the relation between the angle of incidence θ_i and the angle of transmission θ_t set by Snell-Descartes law, a study of how R evolves as n_2 changes can be performed, setting the fiber refractive index to be $n_1 = 1.46$ (close to that of fused silica).

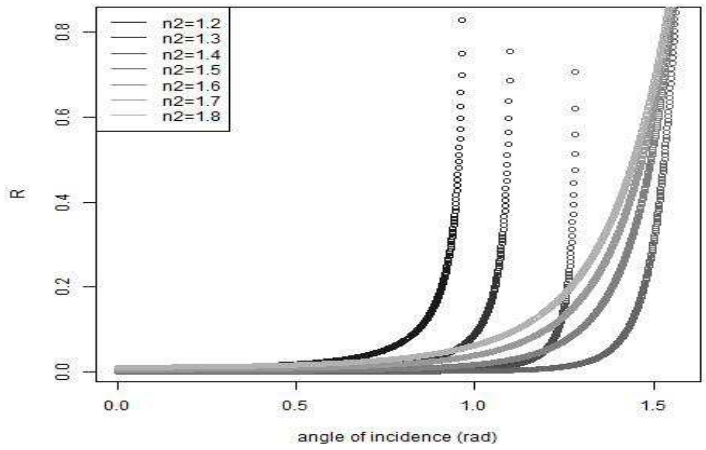

Figure 3.2.12 – Dependence of the reflectivity R on the value of the refractive index within the confinements of the taper, $\boldsymbol{n_2}$.

For $n_2 < n_1$, then there is a critical angle θ_c (no transmission for $\theta_i > \theta_c$), which increases as n_2 also increases. As larger values for n_2 are approached, then there is no critical angle; one might notice that, in this regime (the one we are interested in, since, typically, $\Delta n > 0$), for a given θ_i, the reflectivity increases as n_2 becomes larger. This simplified analysis goes to explain why the average power of the reflected light increases during the fabrication process: the refractive index of the portion of the fiber being actively transformed during this process increases, leading to a higher reflectivity.

It might be of interest to compare the spectra for transmission and reflection as the end of the fabrication process is reached to realize that interference is mainly a characteristic of the transmitted light.

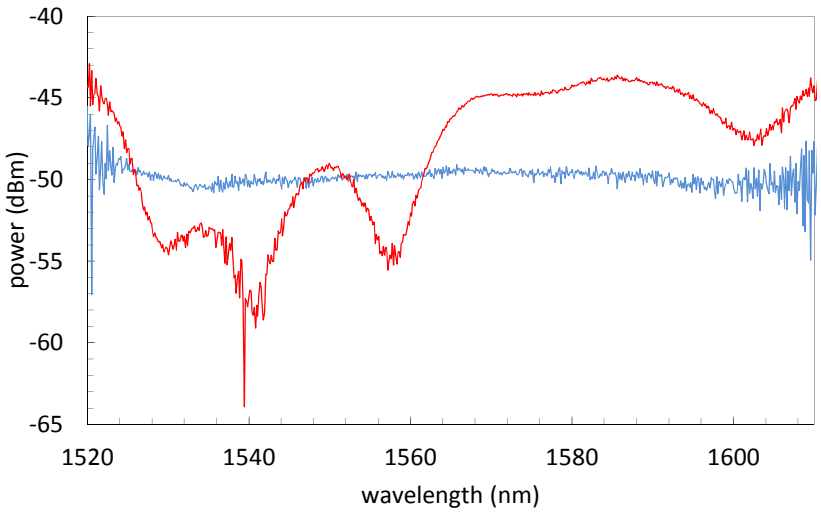

Figure 3.2.13 – Transmission and reflection spectra (P = 1.5 W for 4 min and then P = 1.4 W for 40 min; m = 2 g). Red (transmission), blue (reflection).

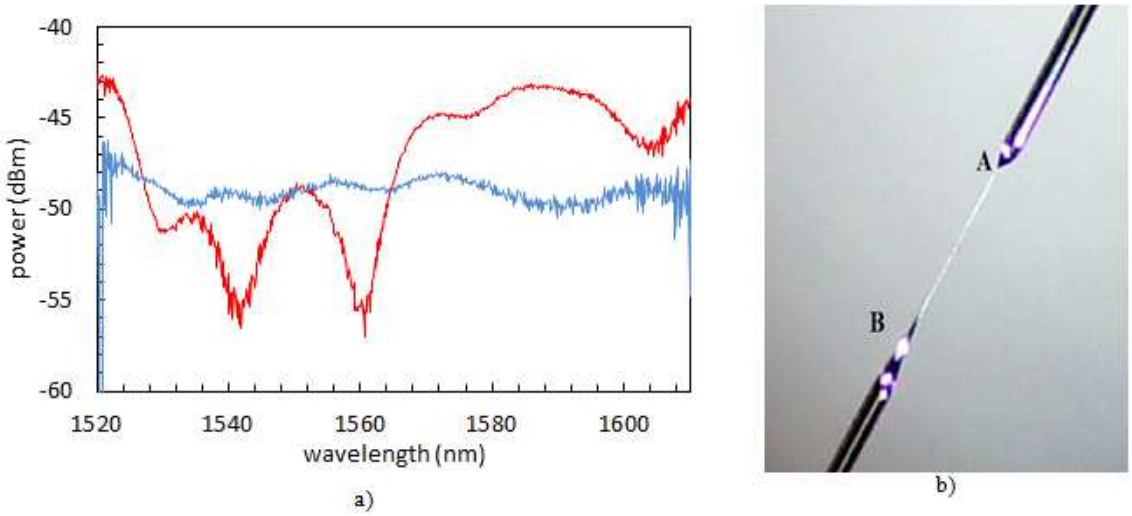

Figure 3.2.14 – a) Transmission and reflection spectra. Red (transmission), blue (reflection). b) Thin taper, with 960 μm; (P = 1.5 W for 4 min and then P = 1.4 W for 50 min; m = 2 g). Light travels from A to B.

3.3 Conclusion

Optical fiber tapers are fabricated resorting to attaching a weight to the fiber, placing it under extra mechanical stress, which is proportional to the weight mass. As weights with

larger weights are used, the fabrication process becomes faster and the taper fiber length increases. The interference spectrum gets sharper with deeper fringes, thanks to a smaller waist diameter that leads to a more effective interference between light traveling along the core and traveling along the cladding, but also suffers more significant losses.

Analyzing the time evolution of the transmission spectrum, it is possible to detect a specific trend concerning the position of the fringes. As time goes by, for a taper fabricated with a laser power P = 1.5 W and an attached mass equal to 4 g, the two fringes in the interference spectrum continuously move towards shorter wavelengths, but at different time rates. A linear relation between wavelength shift and time is obtained for both resonant loss peaks. If one assumes acceptable to establish a linear relation between time and the variation of a given parameter, such as refractive index that is known to change during the fabrication process, especially in the case of small variations, then the potential of a taper to work as a sensor is reinforced. The different time rates may allow to infer different sensitivities for each fringe, important for physical parameter discrimination.

The fact that laser light is always shining upon the fiber at the same spot creates longitudinal asymmetry. In order to understand the impact on light propagation along the fiber, the reflected light is also analyzed. It becomes apparent that the potential for interference is only present for the transmitted light, even though, as the fabrication process takes place, the reflected power increases, accounting for part of the losses observed for the transmitted light.

4. Taper Fabrication II – applied mechanical stress using PC controlled motorized stages

4.1 Experimental setup

The experimental setup used to fabricate tapers resorting to applied mechanical stress using motorized stages is very similar to the one devised to fabricate tapers using attached weights to the optical fiber. The only modification worth mentioning is the introduction of a AEROTECH control unit, responsible for establishing communication between a PC, with the required control software (NLoad) and a LabVIEW routine installed, and the motorized stages. The use of the motorized stages represents a boost in the setup versatility as different kinds of tapers can be obtained assigning different speeds to each stage **[58]**. Besides this, the implemented routine also allows for the modification of the taper length.

4.2 Analysis of the experimental results

The efforts employed at this stage of the fabrication process were focused on determining qualitatively the influence of three major parameters on the taper shapes as well as on the transmission spectra. These parameters are the Pulse Width Modulation of the laser, PWM (as shown before, with a known and well characterized relation with the actual power delivered onto the fiber by the laser), the speed differential between the motorized stages, SD, and the speed magnitude, SM. All the subsequent values regarding these speeds are written in units of 100 $\mu m/s$.

Five different PWM are chosen, keeping both the SD and SM constant equal to 6 and 14, respectively. The PWM values under scrutiny are 10%, 15%, 20%, 25%, 30%. Larger values for the PWM are not considered since the result of such choice of values would lead to a very thin taper with a considerably abrupt transition region (in some cases, the associated power is large enough to almost immediately break the fiber). The main identified trends point to an increase in the average power loss as larger values for the PWM are considered. The taper waist diameter tends to decrease as larger PWM are employed.

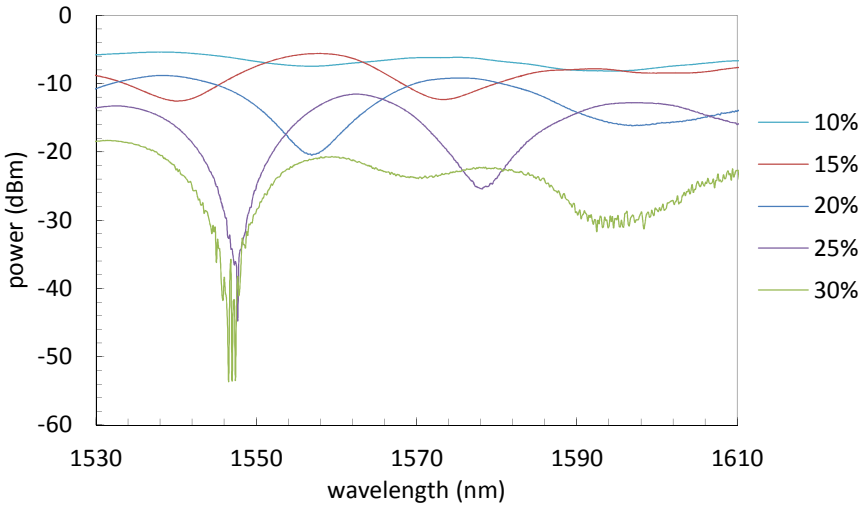

Figure 4.2.1 – Taper transmission spectra for different PWM (10%, 15%, 20%, 25%, 30%). SD = 6, SM = 14.

The graphic in Figure 4.2.1 emphasizes the initially noticed trend that losses increase as the PWM also increases. As the maximum PWM considered is approached, interference becomes more apparent, as one would expect given the thinner profile of the taper waist, giving rise to a more effective interaction between light traveling along the core and the cladding. However, accompanying this fact, as well as the increasing losses, a Fabry-Pérot-like interference pattern sets in for 30%.

An interesting result comes up when the average transmitted power, P_{av}, is determined for each PWM and the relation between these variables can be traced: a linear regime is obtained.

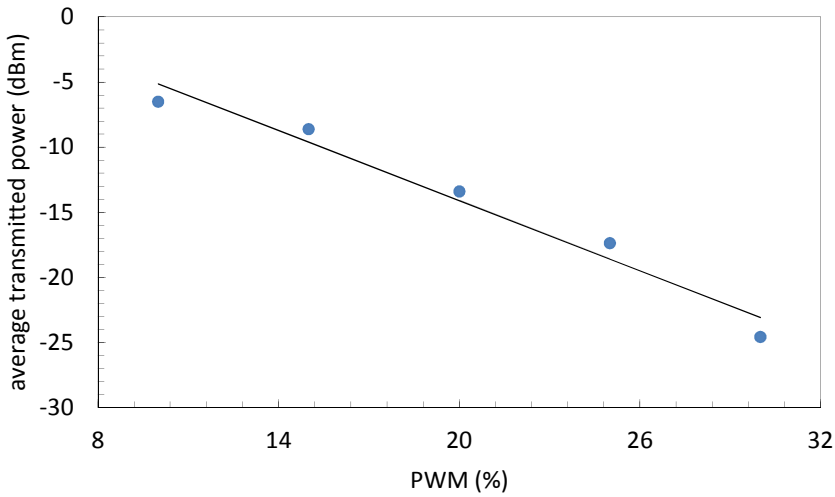

Figure 4.2.2 – Average transmitted power vs .PWM (SD = 6, SM = 14). Line (linear fit).

As was inferred through the analysis of the graphic in Figure 4.2.1, to increasing PWM correspond smaller taper waist diameters, leading to a more distinct interference pattern. Indeed, that is the conclusion drawn from the observation of the tapers profiles.

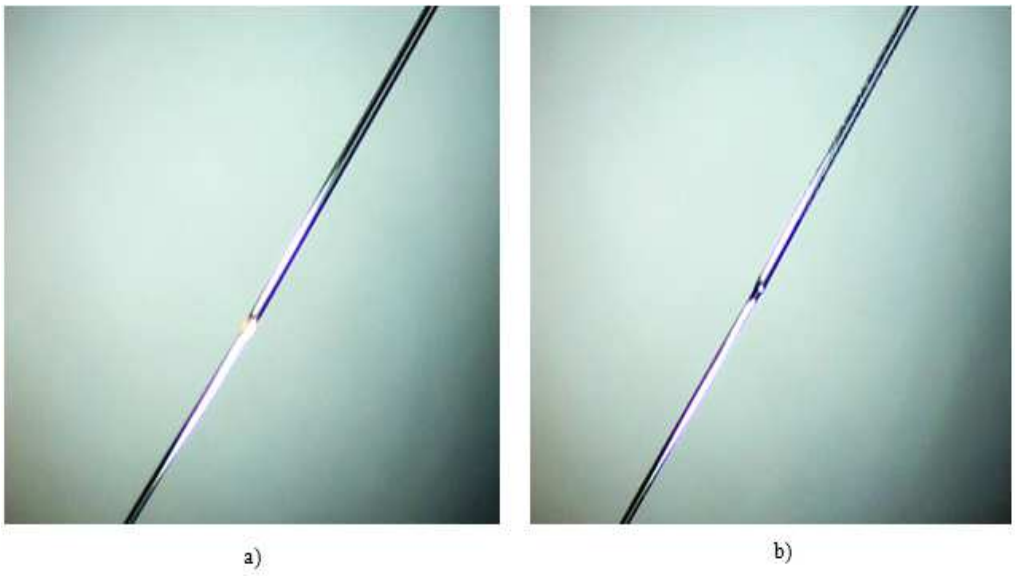

Figure 4.2.3 – Taper spatial profile for different PWM: a) – 10%; b) – 25% (SD = 6, SM = 14).

Another major concern is related to the longitudinal asymmetry that was obvious during the fabrication of tapers using an attached weight. The motorized stages should contribute to mitigate this problem as the laser beam no longer hits the fiber at the same spot throughout the entire fabrication process. Such expectation is fulfilled as can be confirmed by analyzing the taper shape for a device fabricated with PWM = 15%: the longitudinal asymmetry is clearly attenuated and the transition regions become smoother.

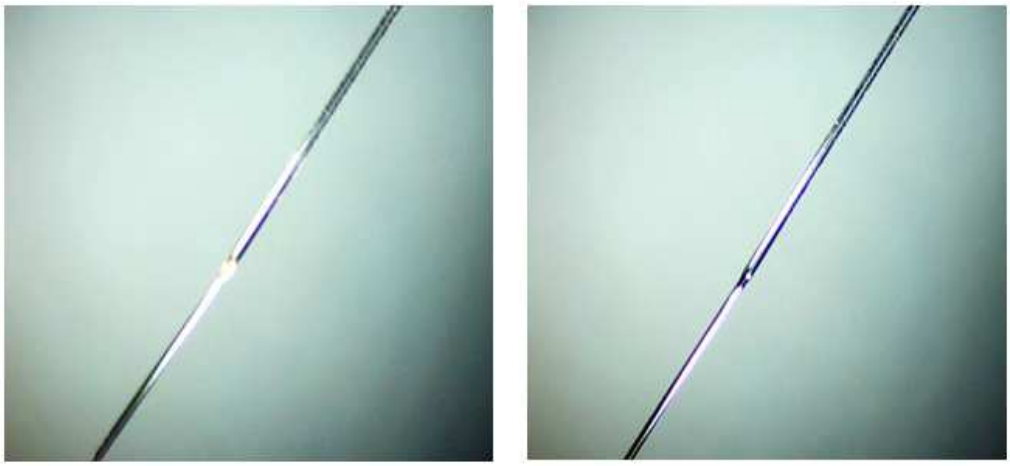

Figure 4.2.4 - Taper spatial profile for PWM = 15%: a) input end of the taper; b) output end of the taper.

A more detailed examination of the enhanced longitudinal symmetry is achieved using an optical microscope to inspect the shape of a taper fabricated with PWM = 20%, SD = 6 and SM =14. Figure 4.2.5 shows two transition regions with a relatively smooth profile, much less abrupt than the typical profile resulting from taper fabrication using weights. The longitudinal asymmetry is not completely cleared out of the way, as can be confirmed looking at the image on the right-hand side of Figure 4.2.5. This observation can explain why the transmission spectra, obtained injecting light into the taper through different ends of the device, are different. Despite registering a maximum deviation of only 13% concerning the loss peak wavelengths, the minimum power associated to a given loss peak wavelength is significantly different, when both spectra are compared. This is a consequence of having a transition region with a slightly more abrupt profile, responsible for larger power losses and deeper fringes. The reflection spectra reveal that the power

losses that take place due to reflection at the interface between the unchanged portion of the fiber and the tapered region are very small; this can be a hint that the fabrication process, quicker in the case in which motorized stages are used when compared to the use of weights, leads to a smaller change in the optical fiber refractive index, allowing most of the light to be transmitted through the aforementioned interface. The losses are then mostly due to coupling from the core to the cladding and from there on to the surrounding environment.

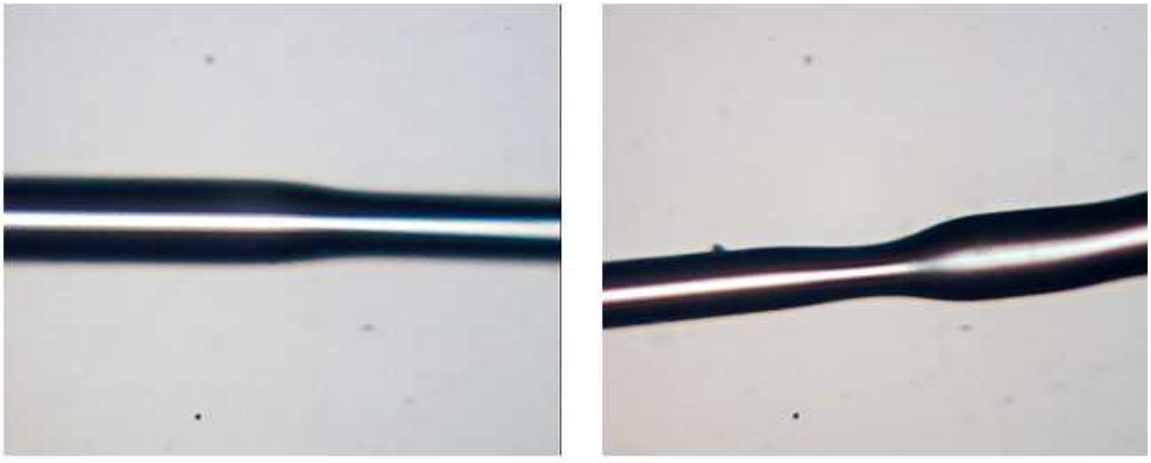

Figure 4.2.5 - Taper spatial profile for PWM = 20%, SD = 6, SM = 14.

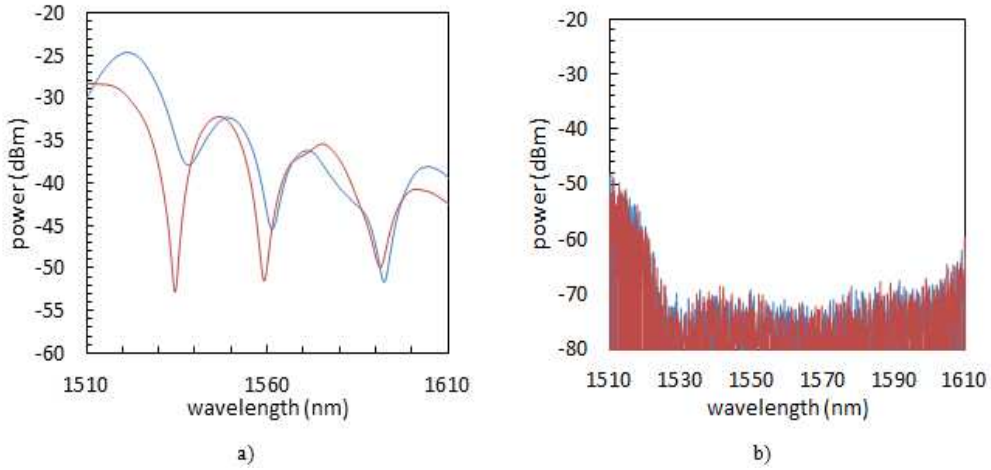

Figure 4.2.6 – a) Transmission spectra obtained injecting light through the taper end in Figure 4.2.5 a) (blue line) and injecting light through the taper end in Figure 4.2.5 b) (red line); b) Reflection spectra obtained injecting light through the taper end in Figure 4.2.5 a) (blue line) and injecting light through the taper end in Figure 4.2.5 b) (red line).

The process to evaluate the taper characteristics proves to be also fruitful in testing its potentialities as a sensor. When curvature and stress are applied to the freshly-made taper, the corresponding interference pattern reveals to be quite responsive, in what concerns average transmitted power and the minimizing wavelengths. For one particular case, the pattern suffers quite the change after introducing curvature, with the appearance of new interference fringes: curvature can definitely change the interference conditions. Besides, the average power also significantly drops. The taper was produced with PWM = 10%, SD = 4 and SM = 6 (first values to be tested).

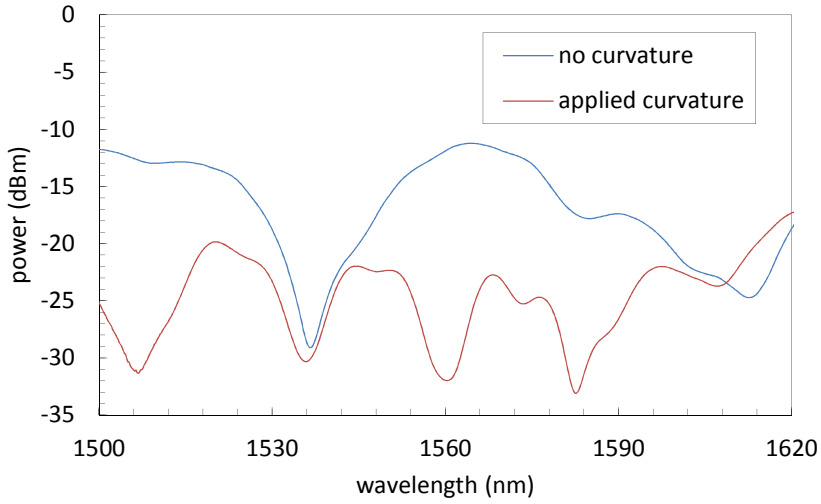

Figure 4.2.7 – Transmission spectra for no curvature applied (blue line) and curvature applied (red line).

The new tested values for the three major parameters also produce interesting results regarding the evolution of P_{av} with the PWM. These results are in overall good agreement with the previously analyzed data (SD = 6 and SM = 14): as the applied PWM increases, P_{av} decreases, following an approximately linear profile. The rate γ at which P_{av} decreases is smaller for this new set of values.

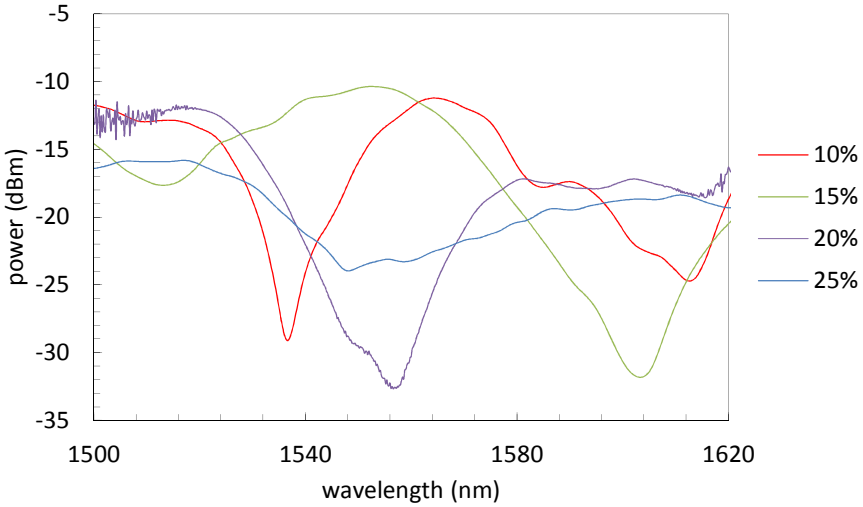

Figure 4.2.8 - Taper transmission spectra for different PWM (10%, 15%, 20%, 25%). SD = 4, SM = 6.

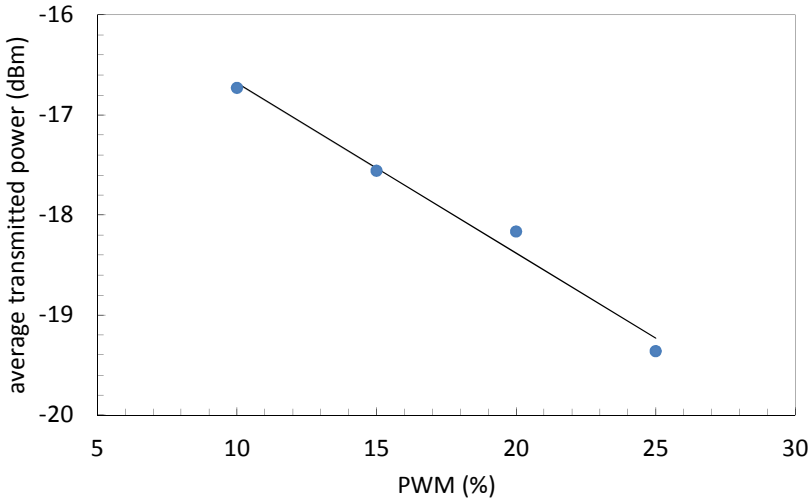

Figure 4.2.9 - Average transmitted power vs .PWM (SD = 4, SM = 6). Line (linear fit).

A quick comparison between the transmitted spectra for different PWM obtained in the two cases under study reveals that, in the first one, the number of fringes is always the same and equal to two, even though the corresponding wavelengths change, while in the second case, for larger PWM, only one fringe appears, and for 25 %, the interference pattern reveals a not so effective interaction between the two interfering light beams (along the core and cladding).

The fact that SD decreases results in smaller tension applied to the fiber, while the fact that SM decreases leads to a longer exposure time elapsed during the fabrication process. These two modifications lead to a smaller rate γ at which P_{av} decreases, meaning that despite a longer exposure time interval, ETI, the fact that the applied tension is reduced is pivotal in explaining why such change in the value of γ takes place. For PWM = 10 %, P_{av} is smaller in the second case, meaning that the longer ETI is critical in the overall contribution to the modification of the fiber shape, consequently to the average transmitted power. As one moves to larger PWM values, P_{av} decreases faster for the first case and for PWM = 25 %, P_{av} is approximately the same for both sets of values for the fabrication parameters: in this range of values for PWM, the larger applied tension in the first case becomes instrumental in setting up the conditions (through optical fiber shape modification) that ultimately have as a consequence the more significant decrease in P_{av}.

Five different SM are chosen. The PWM and SD are kept constant and equal to 10 % and 6, respectively. The SM values under scrutiny are 8, 10, 12, 14 and 16. The variation in SM can be seen as a variation in the ETI: for example, as SM increases, the ETI decreases. For this reason, larger SM values are not considered, since the corresponding ETI´s are quite short, resulting in an only slight change of the fiber shape which does not give rise to an effective light interference. As shorter ETIs are attempted, P_{av} increases, in good agreement with the expectation that these shortened exposure times leave the fiber diameter at the region of laser incidence almost unchanged, supported by the photographs in Figure 4.2.11. The curious aspect of the analyzed data is the sudden increase in P_{av} when one moves from SM = 10 to SM = 12. From then on, P_{av} increases slightly.

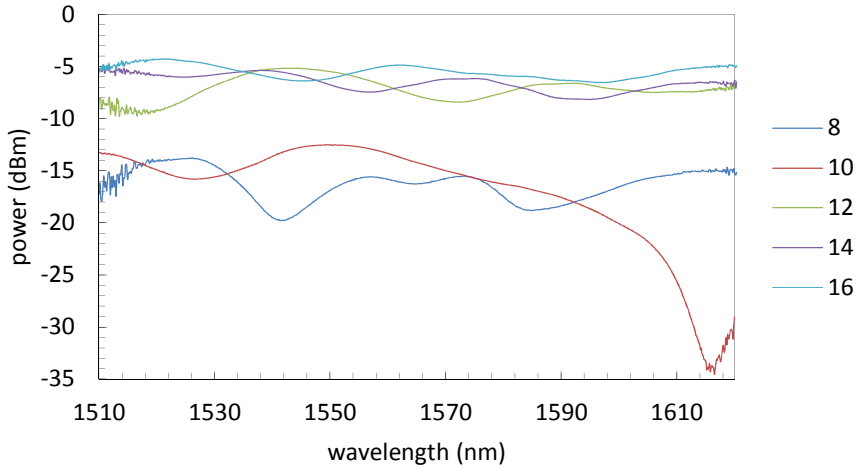

Figure 4.2.10 - Taper transmission spectra for different SM (8, 10, 12, 14, 16). SD = 6, PWM = 10 %.

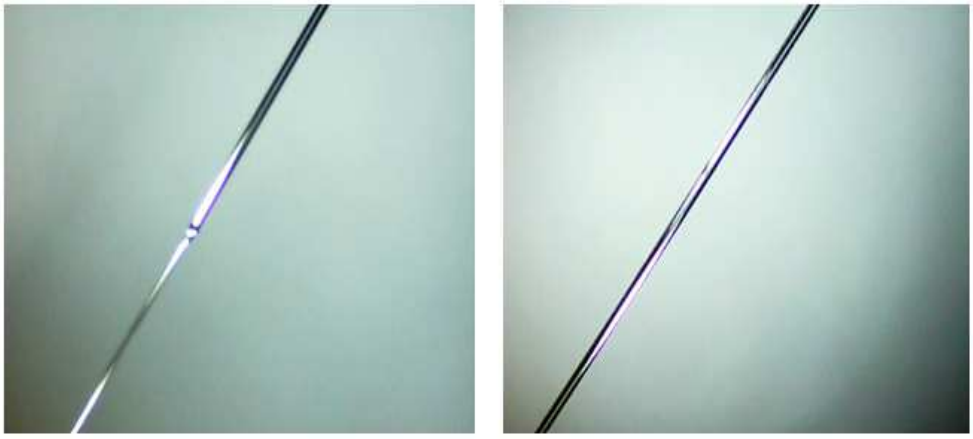

Figure 4.2.11 – Taper spatial profile for different SM: a) 8; b) 14 (SD = 6, PWM = 10 %).

Four different SD are selected. The PWM is kept constant and equal to 10 %. The SD was altered by changing the speed assigned to the y-stage, which means that the ETI also changes. The SD values under scrutiny are 2, 4, 6 and 8. Larger values for SD are not considered since the associated mechanical stress the fiber is subjected to can easily cause it to break or present a considerable mechanical fragility. P_{av} remains approximately constant for SD = 2,3,6 and drops for SD = 8. The chosen strategy to evaluate the impact of different SD on both the shape of the taper and on the transmitted spectrum implies a change in the applied tension and in the ETI: for larger SD, the induced mechanical stress increases, but the ETI becomes shorter. The result of these simultaneous modifications is not easy to predict since a larger mechanical stress contributes to a more pronounced reconfiguration of the taper shape, which tends to be counterbalanced by a shorter ETI. This balancing act might be responsible for the previously mentioned approximately constant P_{av} for SD = 2,3,6, although the interference patterns obtained are significantly different regarding, for example, the position of the fringes, as well as the spatial profiles of the fabricated tapers. Only for SD = 8 does it seem that these simultaneous modifications no longer cancel each other out in terms of the inflicted power losses during fabrication. For increasing SD, the taper waist diameter seems to become smaller, as confirmed by the analysis of the photographs in Figure 4.2.13. A little bit of a more abrupt transition region seems to set in as a result of fabrication conditions that create a thinner tapered region.

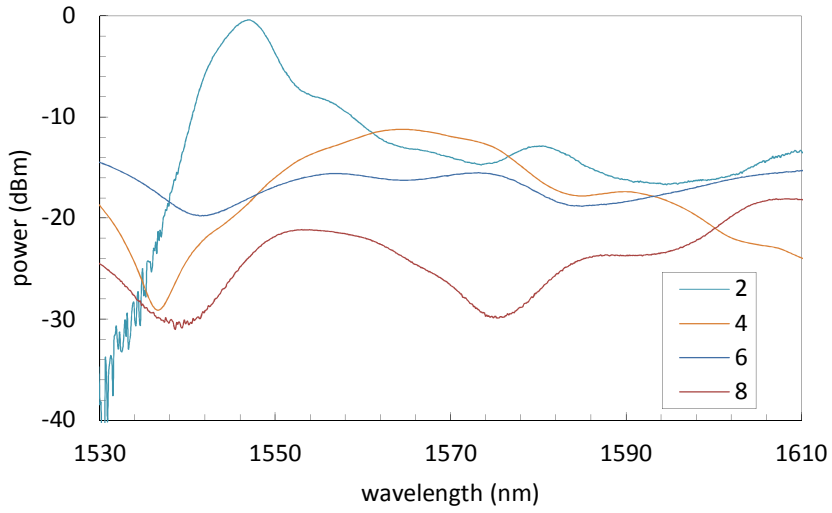

Figure 4.2.12 - Taper transmission spectra for different SD (2, 4, 6, 8), PWM = 10%.

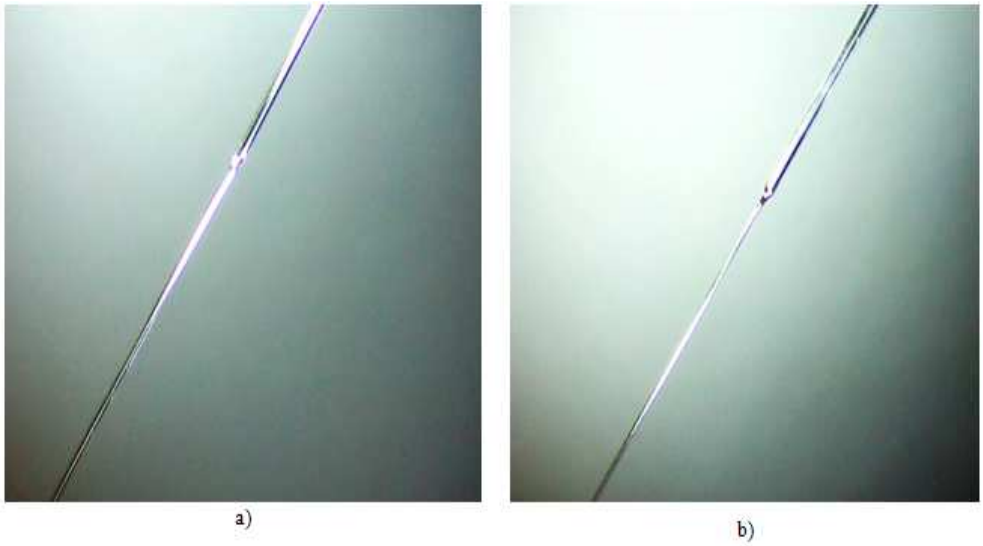

Figure 4.2.13 - Taper spatial profile for different SD: a) 2; b) 8 (PWM = 10 %).

Revaluating all the results obtained so far, the taper with one of the most promising compromises between power losses and the depth of the fringes is obtained resorting to PWM = 25 %, SD = 6 and SM = 14. It is of significant importance to try and evaluate the degree of reproducibility achieved with the proposed setup. In order to do so, three tapers are produced and the respective transmission spectra and shapes evaluated and compared. Their potentiality for use as sensors is also assessed.

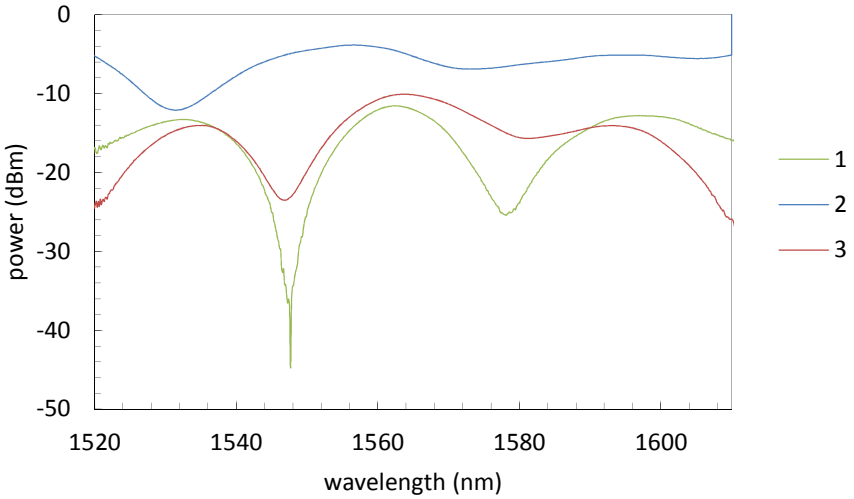

Figure 4.2.14 – Taper transmission spectra for PWM = 25%, SD = 6 and SM = 14.

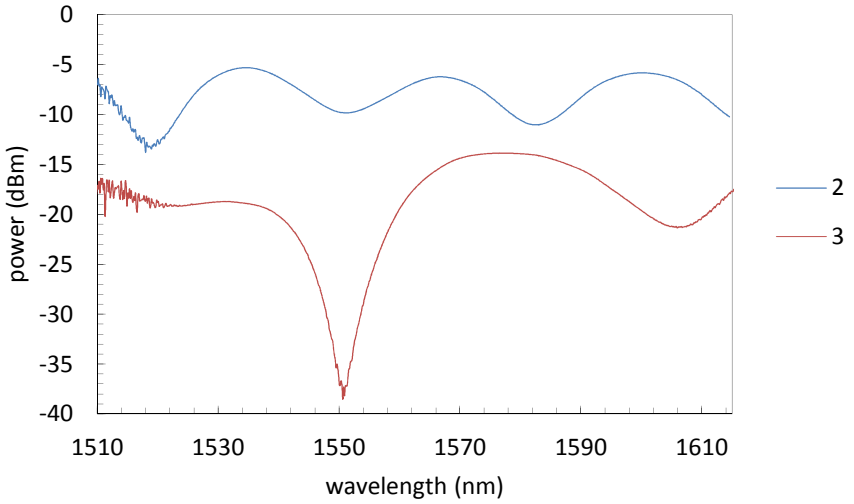

Figure 4.2.15 – Taper transmission spectra for PWM = 25 %, SD = 6 and SM = 14 after applying curvature for tapers 2 and 3.

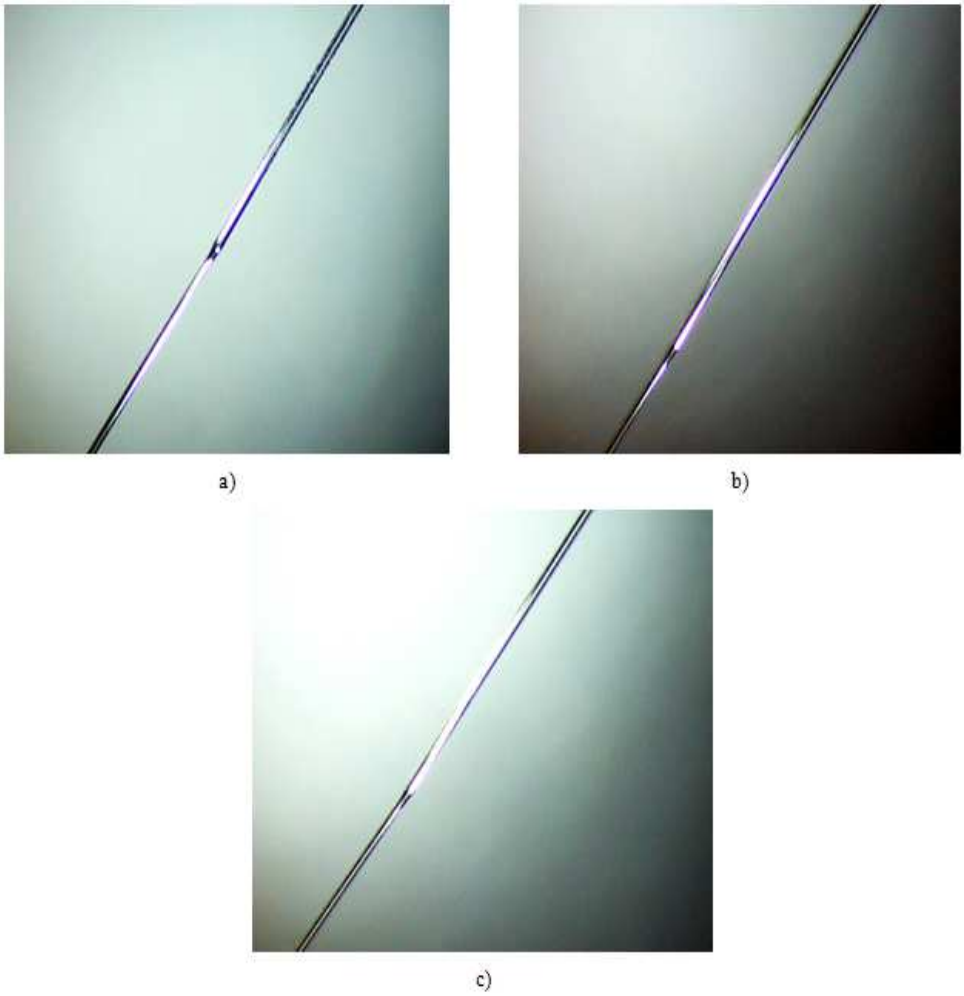

Figure 4.2.16 – Taper spatial profile for three different tapers fabricated with PWM = 25 %, SD = 6 and SM = 14.

The interference patterns show some variability even though the values of the fabrication parameters are kept the same. P_{av} is approximately the same for tapers 1 and 3, -17.38 dBm and -16.40 dBm, respectively, but noticeably changes for taper 2, being equal to -6.31 dBm. The interference conditions also vary, resulting in fringes associated to different minimizing wavelength; taper 1 exhibits deep fringes, which become progressively less deep for tapers 3 and 2. All the tapers fabricated under these conditions show a reasonable sensitivity to variations in external parameters, namely changes in curvature and strain. Besides an obvious alteration of the interference conditions, especially for taper 2 with the appearance of new fringes, curvature also promotes a variation in P_{av}, with 20 % and 13 % for tapers 2 and 3, respectively. The depth of the fringes in the

interference pattern of taper 3 clearly increases and, for example, the minimizing wavelength corresponding to the fringe located towards shorter wavelengths (deeper fringe) shifts from 1546.84 nm to 1550.62 nm. The shape of the tapers does not change significantly. The transition region is quite smooth for all the tapers produced.

4.3 Conclusion

The variations of the three major fabrication parameters PWM, SD and SM produce identifiable changes in the tapers transmission spectra and shapes.

As PWM increases, P_{av} decreases, following an approximately linear behavior. The taper waist diameter is reduced and the depth of the fringes increases, as a result of a more effective interference between light traveling along the core and light traveling along the cladding. The produced tapers present good sensitivity when curvature is applied, in terms of the P_{av}, but also in terms of the interference conditions, with the appearance of new interference fringes.

As SM increases, the ETI decreases and P_{av} tends to increase as the taper waist diameter becomes larger; interference is not as effective and the depth of the fringes decreases.

Probing larger SD values, the mechanical stress the optical fiber is under increases and P_{av} decreases and the taper becomes thinner.

The longitudinal asymmetry, an issue in the fabrication using weights attached to the fiber, seems to be mitigated using this strategy, as the observation of the tapers spatial profile reveals a smoother transition region.

The reproducibility of this setup is tested for a good set of values for PWM, SD and SM, equal to 25 %, 6 and 14, respectively. For these values, a good balance between power losses and the depth of the fringes, intimately related with the strength of the interference, is met. The reproducibility seems to be compromised since both the transmission spectra as well as the tapers profiles differ from one another. The implemented setup can still accommodate same modifications in order to ensure better reproducibility.

5. Characterization of the tapers as sensors

5.1 State-of-the-art

The simultaneous variation of external parameters, such as temperature, curvature and applied strain, which unavoidably takes place outside a controlled environment, has driven much of the work developed in optical fiber sensing. Several devices have been proposed to overcome this hindrance and more exactly determine the impact of the variation of a single external parameter on the characteristics of the light that interacts with said devices.

A long-period grating (LPG) fabricated with UV laser radiation is tested as a strain-independent temperature and curvature sensor with sensitivities $-164\ \mathrm{pm/℃}$ and $-14\ \mathrm{nm/m^{-1}}$, respectively **[60]**. CO_2 lasers have also been used to fabricate these structures **[61-63]**. The reported sensitivities are $-7.6\ \mathrm{pm/\mu\varepsilon}$ and $3.91\ \mathrm{pm/℃}$, for a LPG inscribed in a photonic crystal fiber (PCF) **[61]**, which renders the device good for strain sensing since the temperature sensitivity is rather small; a larger temperature sensitivity is also reported and equal to $-130\ \mathrm{pm/℃}$ when the LPG is inscribed in a standard single-mode SMF-28 fused silica optical fiber **[63]**.

Taper fabrication using a CO_2 laser has been successfully attempted and thoroughly characterized **[64, 65].** Tapers resulting from this fabrication technique or others can also be used as sensors **[20, 22, 24, 66-68]**. Tapers are fabricated using a butane flame burner to heat the fiber **[20]**; the largest temperature sensitivity is $10\ \mathrm{pm/℃}$ and the sensitivity to strain is equal to $95\ \mathrm{pm/\mu\varepsilon}$. An optical fiber curvature sensor based on two low-loss tapers in tandem is reported **[22]**. Another curvature sensor relying on a Mach-Zehnder interferometer created by two cascading abrupt-tapers is examined **[24]**. The device presents low sensitivity to temperature and curvature sensitivities equal to $-13.176\ \mathrm{nm/m^{-1}}$, from $4.8\ \mathrm{m^{-1}}$ to $6.38\ \mathrm{m^{-1}}$, and $-25{,}946\ \mathrm{nm/m^{-1}}$, between $6.48\ \mathrm{m^{-1}}$ and $7.98\ \mathrm{m^{-1}}$. A taper is fabricated in a microstructured optical fiber (MOF) with a silica core surrounded by air holes arranged in a hexagonal pattern **[66]**; the temperature sensitivity is $12\ \mathrm{pm/℃}$ ($200 - 1000\ ℃$). A PCF tapered fiber, spliced at both ends to a single-mode fiber (SMF), is produced to obtain a temperature-independent curvature sensor, with sensitivities $2.81\ \mathrm{dBm/m^{-1}}$ ($0.36 - 0.87\ \mathrm{m^{-1}}$) and $8.35\ \mathrm{dBm/m^{-1}}$ ($0.87 - 1.34\ \mathrm{m^{-1}}$)

[67]. Two bulge tapers are fabricated in series (by a fusion splicer) also in order to create a Mach-Zehnder interferometer **[68]**; the obtained sensitivities for curvature are $-31.821\ \mathrm{nm/m^{-1}}$ ($4.29 – 4.98\ \mathrm{m^{-1}}$) and $-17.051\ \mathrm{nm/m^{-1}}$ ($4.98 – 5.59\ \mathrm{m^{-1}}$) while the sensitivities for temperature are quite small, being the largest $4.2\ \mathrm{pm/℃}$, which results in a temperature-independent curvature sensor.

More complex devices are engineered in order to achieve physical parameter discrimination **[69-74]**. A superstructure fiber Bragg grating (SFBG) works both as a FBG and a LPG and can be used as a sensor **[69]**. The result is a transmission spectrum with broad loss peaks due to forward-propagating core modes coupling to forward-propagating cladding modes (LPG mechanism) with narrower loss peaks along the slope of the broad loss peaks due to the fact that forward-propagating modes couple to a backward-propagating mode (FBG mechanism). When the wavelength of the narrower peaks is monitored, the calculated sensitivities are $11.3\ \mathrm{pm/℃}$ and $1.06\ \mathrm{pm/με}$; when the power is monitored, the sensitivities are $0.0261\ \mathrm{dB/℃}$ and $-0.00148\ \mathrm{dB/με}$. A highly sensitive bend sensor with hybrid LPG and tilted fiber Bragg grating (TFBG) has its potential as a sensor evaluated **[70]**. Two mechanisms that lead to light reflection are under investigation: light is first coupled out by the LPG and then recoupled to the backward-propagating core mode by the TFBG; the other possibility is to have light propagating along the core, even after leaving the LPG, coupled out to backward-propagating cladding modes and lastly recoupled back into the core. The difference between the powers associated to each of these mechanisms is registered for different curvatures, giving rise to a sensitivity equal to $2.36\ \mathrm{dB/m^{-1}}$ ($2.5 – 7.2\ \mathrm{m^{-1}}$). Sensitivity to temperature is also assessed and values equal to $-340\ \mathrm{pm/℃}$ and $30\ \mathrm{pm/℃}$ are found for a photosensitive fiber and a standard SMF, respectively. A high-reflectivity FBG is written in a SMF-28 hydrogen loaded fiber by UV laser radiation and spliced together, at both ends, with another fiber, with the peculiarity that one of the splices is misaligned **[71]**. Coupling modes are excited at this misaligned splice and two different kinds of coupling mechanisms are present: the light coupled out of the core and into the cladding at the offset is recoupled into the backward-propagating core mode by the FBG; the light can also be coupled to the backward-propagating cladding modes by the FBG and then recoupled at the offset. The first mechanism is dominant and

the associated power P_1 varies significantly with applied curvature but remains approximately the same with changing temperature. The relation between P_1 and curvature is a polynomial function (second degree). The power associated to the second mechanism does not change much with the variation of external parameters, providing a reference signal. A sandwich structure involving a SMF and a multimode fiber (MMF) of the kind SMF-MMF-SMF is proposed in order to achieve temperature and strain-independent curvature sensing **[72]**. The transmission spectrum exhibits two fringes and the difference in wavelength shift $\Delta\lambda$ is monitored for different curvatures, temperatures and strain. $\Delta\lambda$ is approximately the same for the studied range of temperatures and strain (0 - 200 ℃ and 0 - 1000 με). The curvature sensitivity is $8.7\ \mathrm{nm/m^{-1}}$. Another sandwich structure, this time involving a SMF and a PCF of the kind SMF-PCF-SMF, is investigated **[73]**. The sensitivities are $4.451\ \mathrm{nm/m^{-1}}$ for curvature ($0 - 2.14\ \mathrm{m^{-1}}$) and $7.78\ \mathrm{pm/℃}$ for temperature, meaning that this curvature sensor is temperature-independent. Like in the previously mentioned device, a sandwich structure with the scheme SMF-PCF-SMF is implemented, but now an offset at the second splice is introduced **[74]**. The sensitivity to temperature is $1.9\ \mathrm{pm/℃}$ ($30 - 100$ ℃), rendering the device almost temperature insensitive, and the sensitivity to curvature is $3.046\ \mathrm{nm/m^{-1}}$ ($0 – 1.4\ \mathrm{m^{-1}}$), which is lower than the one determined before for the case without an offset; one would expect this offset to increase the amount of light coupled out to higher order modes and make interference more effective contributing to an enhanced sensitivity. The same configuration is tested without an offset and including a LPG structure in the first portion of SMF responsible for exciting cladding modes; curvature values as small as $0.00004\ \mathrm{m^{-1}}$ can be measured.

The main focus of this characterization is to evaluate the dynamics of the transmission spectrum as the external parameters change, especially when it comes to the wavelengths corresponding to resonant loss peaks and the associated transmitted power. After probing a comprehensive range of values for said external parameters, the relation between the evaluated characteristics of the transmission spectrum and the external parameters can be thoroughly characterized, ultimately allowing the determination of the taper sensitivities.

5.2 Experimental Setup

Taper fabrication is accomplished using an experimental setup including a CO_2 laser and a set of PC controlled motorized stages. The CO_2 laser active medium is excited by an electrical signal with pulse width modulation (PWM) of 25%, corresponding to a laser power of 4.5 W, and a frequency of 10 kHz. The stages parameter values are set so the y-stage and the x-stage have speeds equal to $1400\ \mu m/s$ and $800\ \mu m/s$, respectively. The taper length is set equal to 10 mm. The duration of the fabrication process is 1 minute and 42 seconds.

In order to characterize the tapers fabricated using the CO_2 laser as sensors of curvature and strain, the experimental setup depicted in Figure 5.2.1 is devised. The fiber is fixed onto the manually controlled translation stage as well as onto a block placed at a distance 2*L* from the stage. As the distance between the two points where the fiber is fixed changes, so does the curvature of the portion of the fiber between the stage and the block. If this portion of the fiber contains the taper, then it will also experience a change in curvature. The characterization in strain is performed moving the stage up to the point where there is no curvature, and then beyond that point in order to stretch the fiber and increase the applied strain. The resulting changes in the spectrum of the transmitted light are evaluated using an ADVANTEST Q8384 Optical Spectrum Analyzer (OSA). The broadband light source has a central wavelength of 1550 nm, with a bandwidth of 100 nm and an average power of -30 dBm.

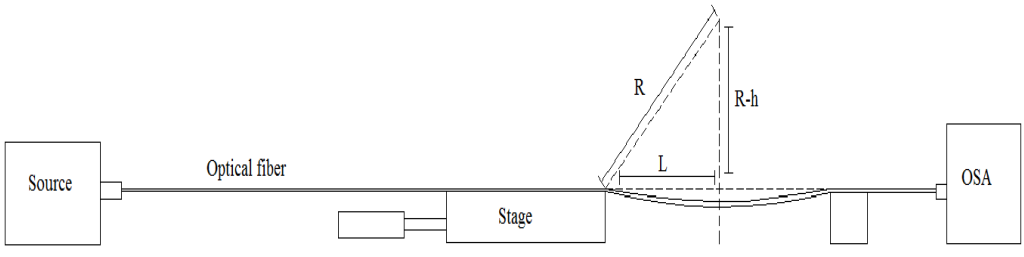

Figure 5.2.1 – Experimental setup for curvature and strain characterization.

The experimental setup devised to perform temperature characterization is similar to the one implemented for strain and curvature characterization except for the inclusion of an oven, responsible for controlling the taper temperature. The manually controlled stage was kept in the setup in order to allow for a quick change of the taper curvature making it easier to tune the characteristics of the transmitted spectrum.

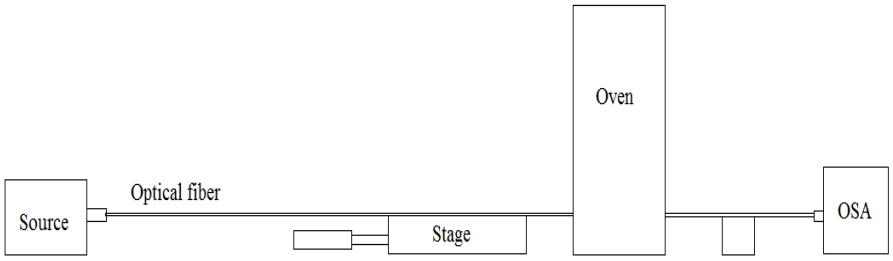

Figure 5.2.2 – Experimental setup for temperature characterization.

5.3 Temperature characterization

The attention was focused on evaluating how the resonant loss peak wavelength λ_m and power of the minima P_m, where *m* identifies the fringe, evolve as temperature changes. For the tapers under study, there is a simultaneous variation both in λ_m and P_m, meaning that both the interference conditions as well as interface characteristics, namely the refractive index difference between core and cladding, change during the characterization process.

The first taper to be tested has two different linear regimes, for the relation $\lambda_2$vs. temperature: one for temperatures between 25 ℃ and 200 ℃ and another between 375 ℃ and 500 ℃; the sensitivities are 64 pm/℃ and 151 pm/℃, respectively. For the range of temperatures between the intervals for which there is linear behavior, interference is no longer as significant as P_m reaches larger values, very close to the average level of power

losses introduced by the taper. As for the evolution of P_m with changing temperature, it does not exhibit as good a linear behavior as the relation λ_m vs. T does, even though, for certain ranges of temperature, it might be acceptable to attempt a linear approximation. The best approximation for the two ranges of temperatures is a polynomial function of the third degree between 25 ℃ and 200 ℃ and of the second degree between 375 ℃ and 500 ℃.

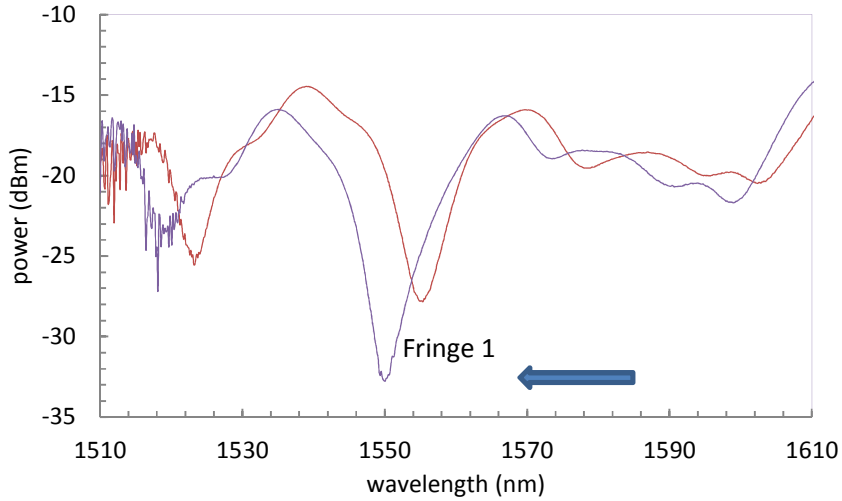

Figure 5.3.1 – Transmission spectrum evolution for decreasing temperature for taper 1. The arrow sets the trend for the resonant loss peak wavelength evolution for decreasing temperature.

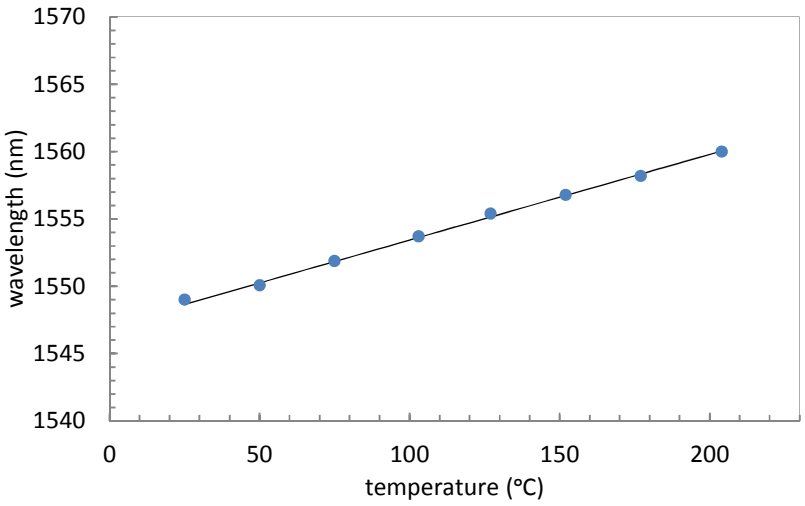

Figure 5.3.2 – Temperature response in wavelength of the interferometric taper 1 using the first wavelength peak between 25 ℃ and 200 ℃. Line (linear fit).

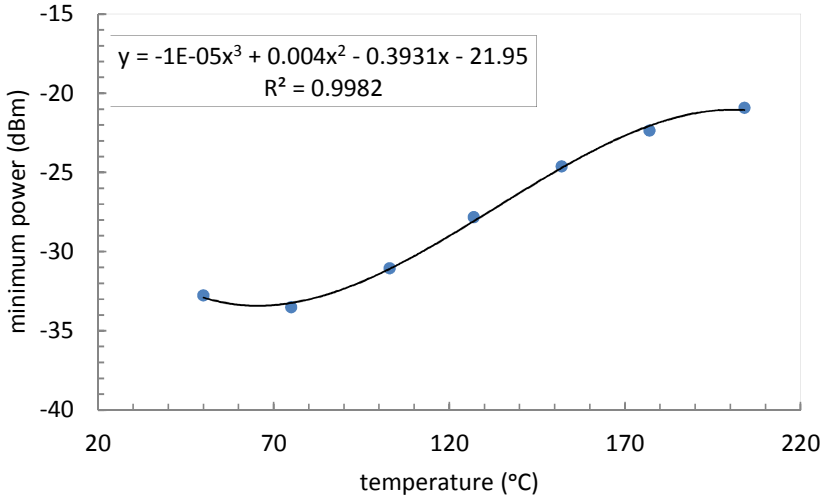

Figure 5.3.3 – Temperature response in power of the interferometric taper 1 using the first wavelength peak between 25 ℃ and 200 ℃.

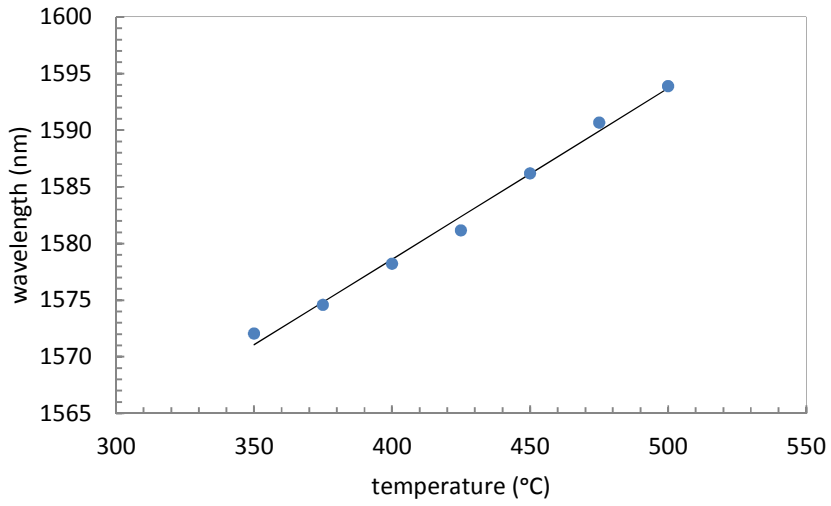

Figure 5.3.4 - Temperature response in wavelength of the interferometric taper 1 using the first wavelength peak between 350 ℃ and 500 ℃. Line (linear fit).

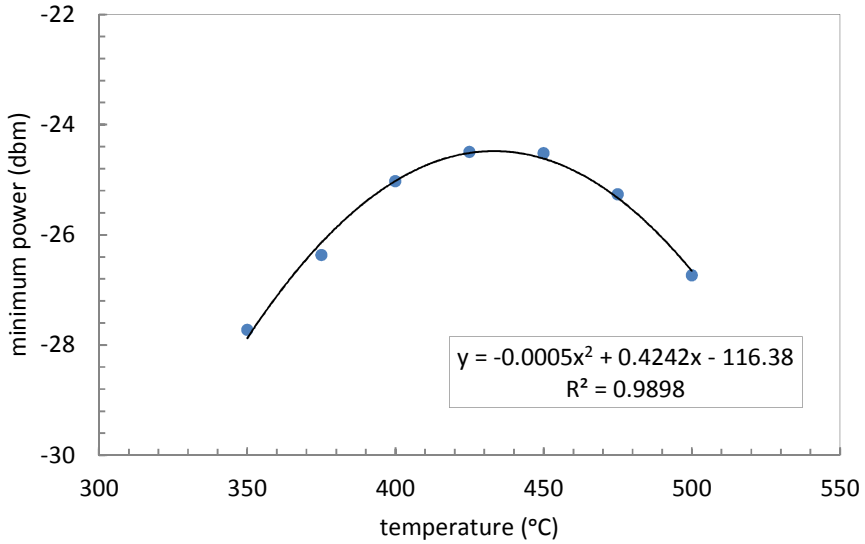

Figure 5.3.5 – Temperature response in power of the interferometric taper 1 using the first wavelength peak between 350 ℃ and 500 ℃.

For the second taper, there is a simultaneous variation in both λ_m and P_m, meaning that both the interference conditions as well as interface characteristics, namely the refractive index difference between core and cladding, change during the characterization process. A good linear behavior is achieved for temperatures between 25 ℃ and 510 ℃

using fringes 1 and 2, located at 1561.12 nm and at 1591.22 nm, for a temperature of 510 ℃, respectively. Fringe 3, located at 1613.90 nm, presents linear behavior for a narrower range of temperatures, only reaching as far as 455 ℃. The sensitivities found for each of the three fringes are, from the shortest to the longest resonant loss peak wavelength, 89 pm/℃, 110 pm/℃ and 81 pm/℃. As for the intensity variation with temperature, a not so easily discernible trend is obtained, meaning the data is not adequate to be used for calibration purposes. Using the other two fringes, fringe 1, located at 1561.12 nm, and fringe 3, located at 1613.90 nm, linear behaviors are also achieved for the same range of temperatures with similar values for the sensitivities.

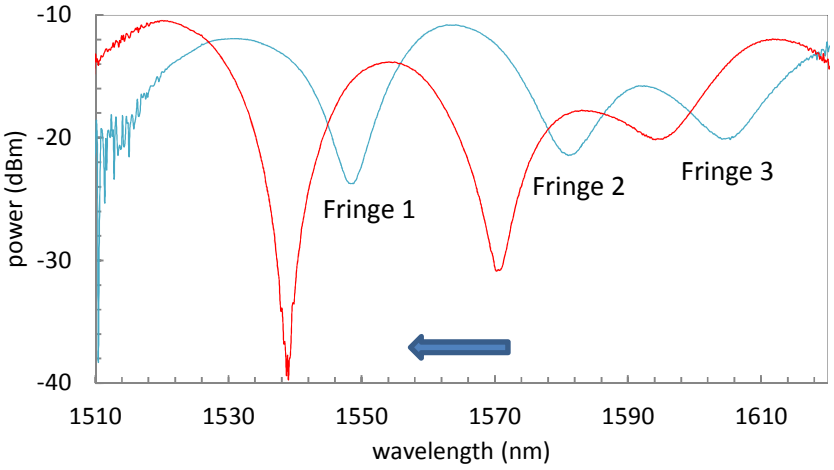

Figure 5.3.6 - Transmission spectrum evolution for decreasing temperature for taper 2. The arrow sets the trend for the evolution of the resonant loss peak wavelength for decreasing temperature.

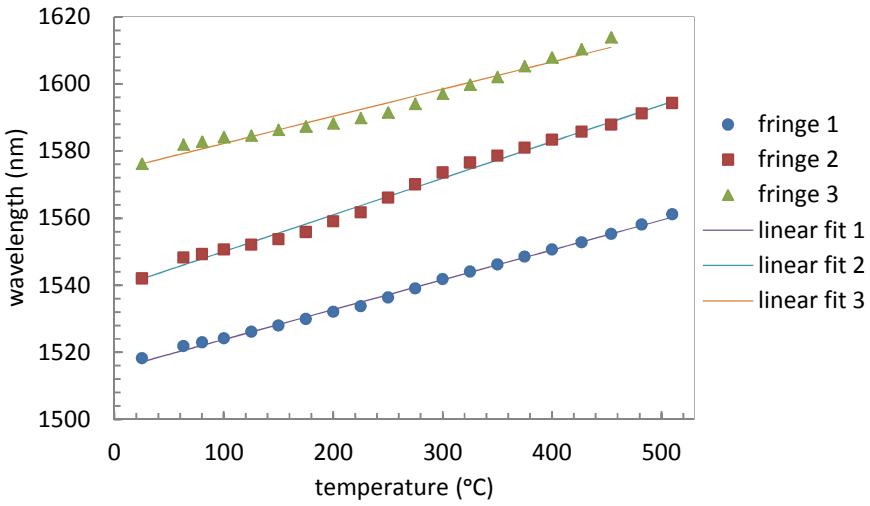

Figure 5.3.7 – Temperature response in wavelength of the interferometric taper 2 using the three fringes in the transmission spectrum between 25℃ and 510 ℃.

Comparing the obtained sensitivities for the different fringes of both tapers, several aspects are worth mentioning, such as the fact that the sensitivity tends to increase as one moves to higher temperatures, result verified for all the fringes in both tapers; for the range of smaller temperatures, between 25 ℃ and 200 ℃, the maximum deviation is found between fringes of the second taper; this result can be a consequence of the fact that one of the fringes monitored is considerably displaced towards longer wavelengths (fringe 3, $\lambda_3 = 1613.90$ nm at $T = 450$ ℃), when compared to the two fringes evaluated for the first taper. If this fringe is disregarded, then the maximum deviation in sensitivity is found between the respective second fringes (both at approximately 1583 nm, at $T = 500$ ℃).

For lower temperatures there is a remarkable proximity between the sensitivities of the fringes associated to shorter wavelengths. These sensitivities tend to increase and distance from each other as higher temperatures are reached. The fact that the determined sensitivities are so close might raise the problem of not being possible to obtain physical parameter discrimination. The inclusion of new fringes, like the third fringe for the second taper, with clearly different sensitivities, can help solve this problem.

The maximum sensitivities are 0.075 nm/℃ (taper 2, fringes 1 and 2) and 0.151 nm/℃ (taper 1, fringe 1), between 25 ℃ and 200 ℃ and between 375 ℃ and

500 ℃, respectively. The deviations are 14% and 47% in the ranges of lower and higher temperatures, respectively (already excluding fringe 3).

Taper 1

		Curvature range (℃)	Sensitivity (nm/℃)
λ_m vs. temperature	Fringe 1	[25; 200]	0.065
		[375; 500]	0.151

Table 1 – Summary of all the sensitivities determined for taper 1.

Taper 2

		Temperature range (℃)	Sensitivity (nm/℃)
λ_m vs. temperature	Fringe 1	[25; 200]	0.075
	Fringe 2	[25; 200]	0.075
	Fringe 3	[25; 200]	0.046
	Fringe 1	[300; 510]	0.090
	Fringe 2	[300; 510]	0.094
	Fringe 3	[300; 450]	0.108

Table 2 – Summary of all the sensitivities determined for taper 2.

Throughout temperature characterization, the fringe located at approximately 1590 nm for a temperature of 510 ℃ moves towards shorter wavelengths as temperature drops and, close to room temperature, settles at approximately 1540 nm. This fringe is identified by λ_2. Fringe 1 reaches wavelength values below 1520 nm. Since this fringe is outside the range of values considered during strain and curvature characterization, the one located at approximately 1540 nm is now identified by λ_1.

5.3 Strain characterization

The evolution of the transmission spectrum as different strains are applied shows that only the power P_1 of the minimum varies significantly, while the associated wavelength λ_1 appears to be rather insensitive to this external parameter, with a sensitivity of 1 pm/με. The resulting changes in temperature due to applied strain are 0.02 ℃/με and 0.006 ℃/με, in the ranges of temperatures between 25 and 200 ℃ and between 375 and 500 ℃, respectively. The maximum deviation from the average of the registered λ_1 is 0.06 %. Bearing in mind how interference occurs in this kind of optical fiber devices, the fact that only P_1 changes considerably means that the strain applied to the taper does not alter the interference conditions, such has the refractive index difference between core and cladding as well as the difference in length of both these light propagating paths. The strain contributes, in the linear regime, to an increase in the transmitted power, or, being more precise, to a reduction of power losses as light travels through the taper. This can be traced to a reconfiguration of the transition region, which may become smoother, resulting in smaller power losses. A linear regime is obtained with a sensitivity of 0.0039 dBm/με, between 0 and 1500 με.

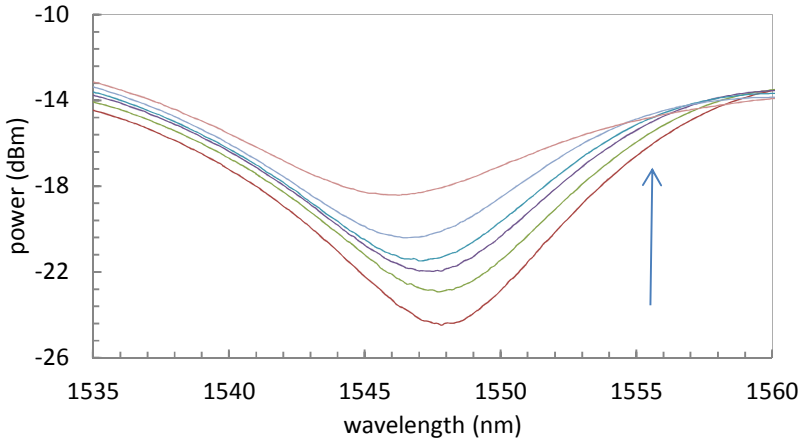

Figure 5.4.1 – Transmission spectrum evolution for increasing strain for taper 1. The arrow sets the trend for the transmitted power evolution as the applied strain increases.

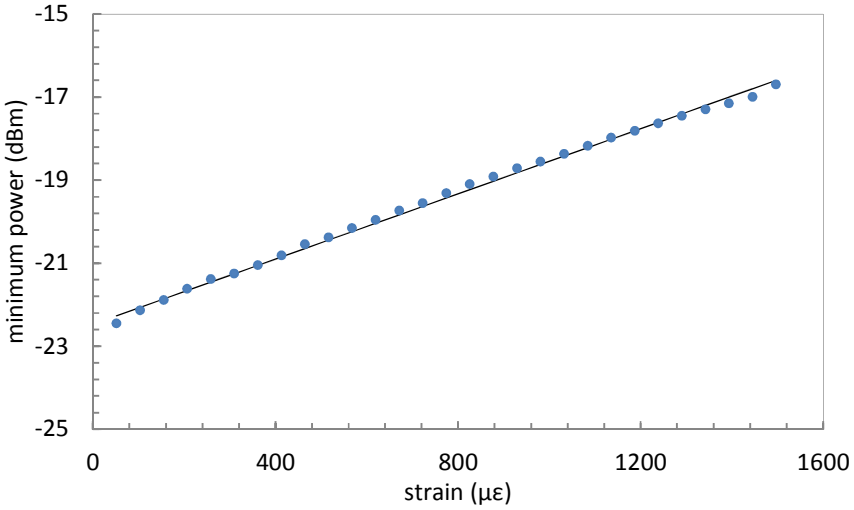

Figure 5.4.2 - Strain response in power of the interferometric taper 1. Line (linear fit).

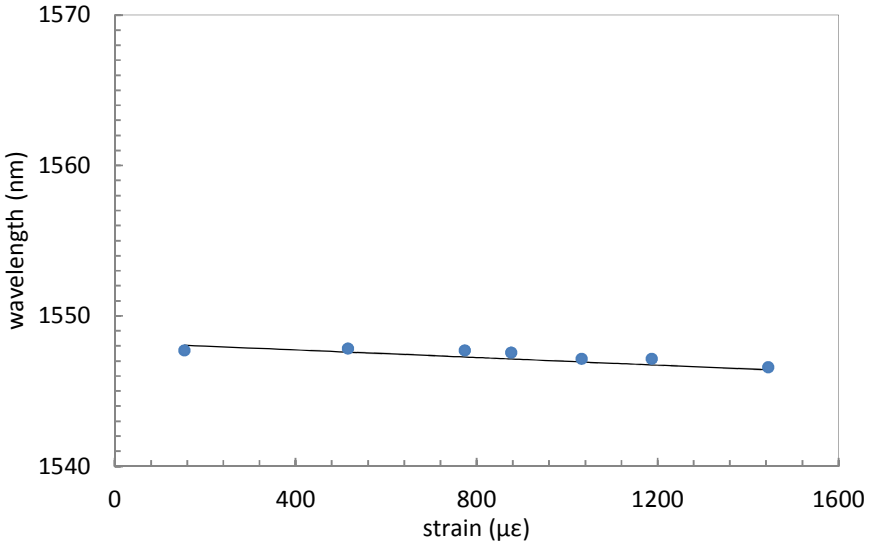

Figure 5.4.3 – Strain response in wavelength of the interferometric taper 1. Line (linear fit).

The second taper shows a messier behavior, since one of the fringes disappears for a given range of applied strain: fringe 3 disappears for applied strain between 642 and 1070 με. Despite this unfortunate event, fringe 3 persists for smaller applied strains and its power P_3 varies linearly. Fringe 2 is characterized by a larger stability and its minimizing power

P_2 also presents a linear relation with the applied strain for a wider range, between 300 and 1100 $\mu\varepsilon$, with a sensitivity of 0.0042 dBm/με. The resonant loss peak wavelength λ_2 remains approximately constant in the entire range of applied strain tested in this characterization process, with a sensitivity of 1 pm/με. The estimated variation in temperature resulting from applied strain is 0.01 ℃/$\mu\varepsilon$. The maximum deviation from the average of the registered λ_2 is 0.04 % .

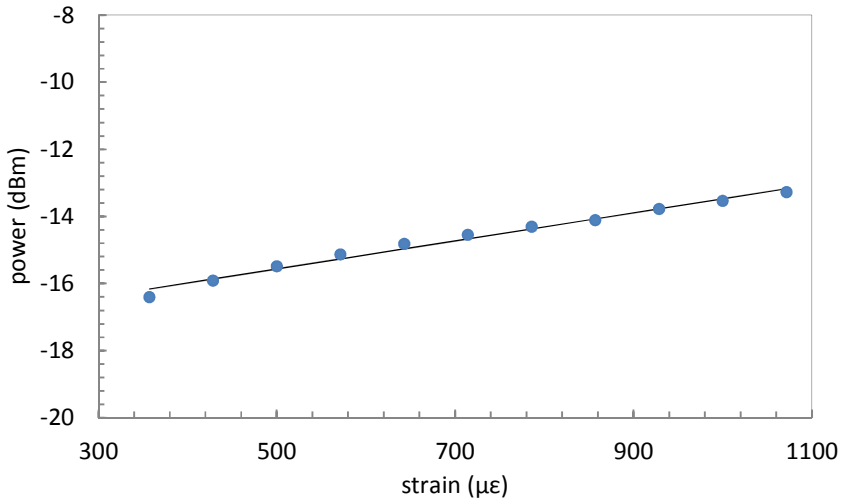

Figure 5.4.4 - Strain response in power of the interferometric taper 2. Line (linear fit).

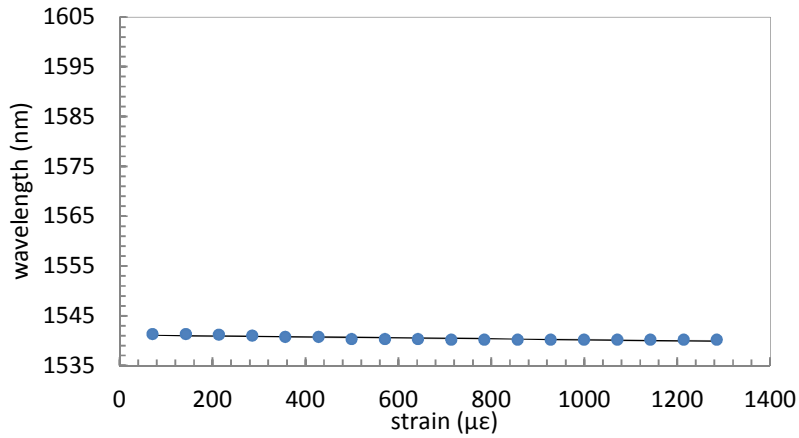

Figure 5.4.5 – Strain response in wavelength of the interferometric taper 2. Line (linear fit).

The sensitivities determined for both tapers are quite similar, presenting a deviation of 4 %. The maximum sensitivity is obtained for taper 2 and is equal to $0.0042\ \mathrm{dBm}/\mu\varepsilon$, but the available range, between 300 and 1100 με, is smaller than the one verified for taper 1, all the way from no strain applied up to 1500 με.

Taper 1

		Strain range (με)	Sensitivity ($\mathrm{dBm}/\mu\varepsilon$)
P_m vs. strain	Fringe 1	$[0; 1500]$	0.0039

Table 3 – Summary of all the sensitivities determined for taper 1.

Taper 2

		Strain range (με)	Sensitivity ($\mathrm{dBm}/\mu\varepsilon$)
P_m vs. strain	Fringe 1	$[300; 1100]$	0.0042

Table 4 – Summary of all the sensitivities determined for taper 2.

5.5 Curvature characterization

The calculation of the curvature can be performed in a rather smooth fashion. If the definition of curvature C is taken to be $1/R$, then it can be explicitly written as a function of the easily measured distances L and h (vertical distance between the middle point of the curved fiber and the completely stretched fiber) **[70]**

$$R^2 = L^2 + (R-h)^2 \Leftrightarrow \frac{1}{R} = \frac{2h}{h^2 + L^2} \tag{5.2.1}$$

The first taper was characterized revealing a considerable sensitivity towards variations in curvature, namely tied to changes in the minimum power P_1, even though no discernible relation between P_1 and curvature can be found. The resonant loss peak wavelength λ_1 exhibits some apparent insensitivity to curvature, with a sensitivity of $1.28\ \mathrm{nm/m^{-1}}$. The estimated variations in temperature resulting from applied curvature are $20\ ℃/\mathrm{m^{-1}}$ and $8\ ℃/\mathrm{m^{-1}}$ in the ranges of temperatures between 25 and 200 ℃ and between 375 and 500 ℃, respectively. The maximum deviation from the average of the registered λ_1 is 0.13 % .

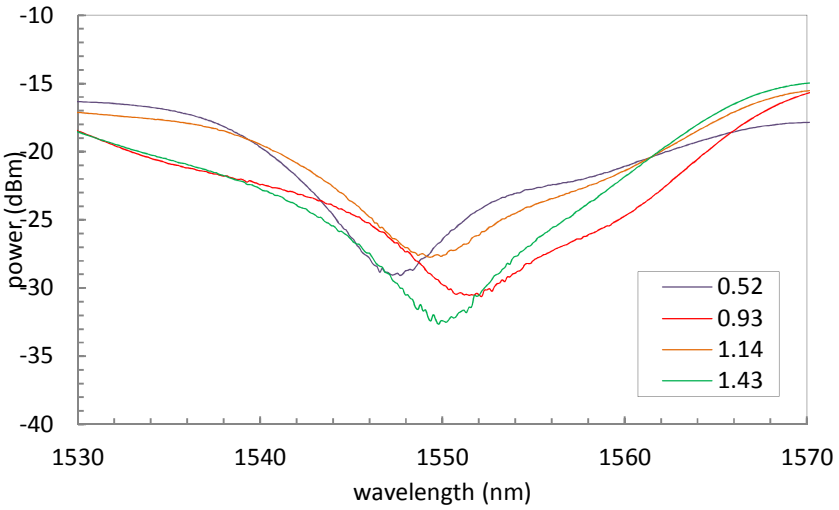

Figure 5.5.1 – Transmission spectra for different applied curvatures for taper 1. The curvature unit is m^{-1}.

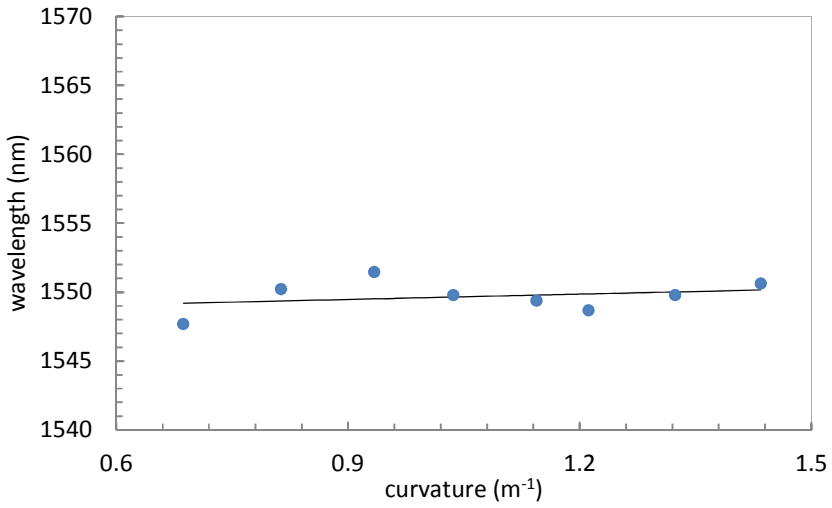

Figure 5.5.2 – Curvature response in wavelength of the interferometric taper 1. Line (linear fit).

When characterizing taper 2, a more easily discernible pattern is followed by the minimum power P_2 as curvature increases. Still, the relation between P_2 and curvature exhibits a rather complex profile: for smaller curvatures, more precisely between no curvature applied and 0.5 m^{-1}, P_2 decreases; once one moves towards larger curvatures, between 0.5 and 1.1 m^{-1}, P_2 increases. The sensitivities for the previously stated ranges of curvatures are $-15.27\ dBm/m^{-1}$ and $13.14\ dBm/m^{-1}$. The changes in λ_2 are not very significant in the curvature range between 0.14 and 0.70 m^{-1}. The estimated variation in temperature resulting from applied curvature is $4.55\ ℃/m^{-1}$. The maximum deviation from the average of the registered λ_2 is 0.02 %.

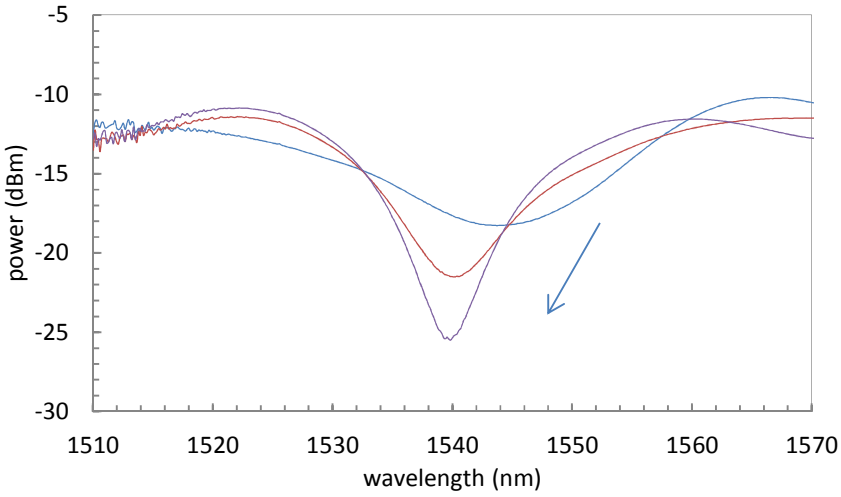

Figure 5.5.4 – Transmission spectra for different applied curvatures for taper 2. The arrow sets the trend for the evolution of the spectra as curvature increases. Range of curvatures [0; 0.5] $\mathbf{m^{-1}}$.

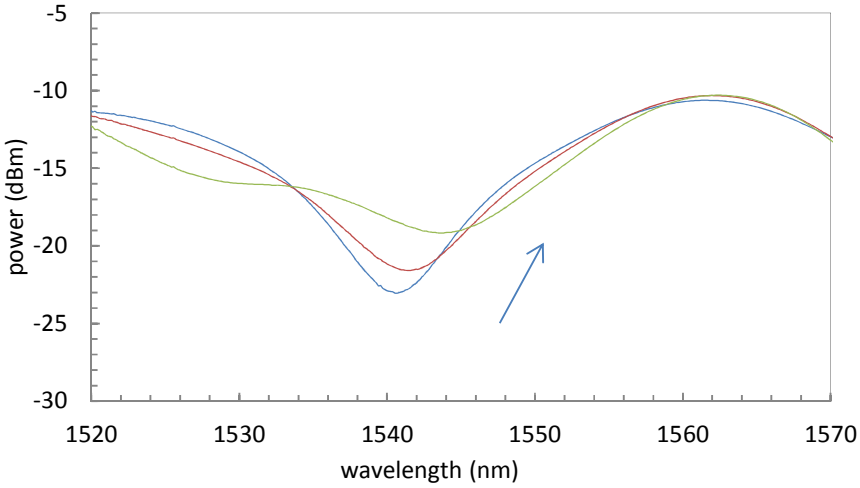

Figure 5.4.5 – Transmission spectra for different applied curvatures for taper 2. The arrow sets the trend for the evolution of the spectra as curvature increases. Range of curvatures [0.5; 1.1] $\mathbf{m^{-1}}$.

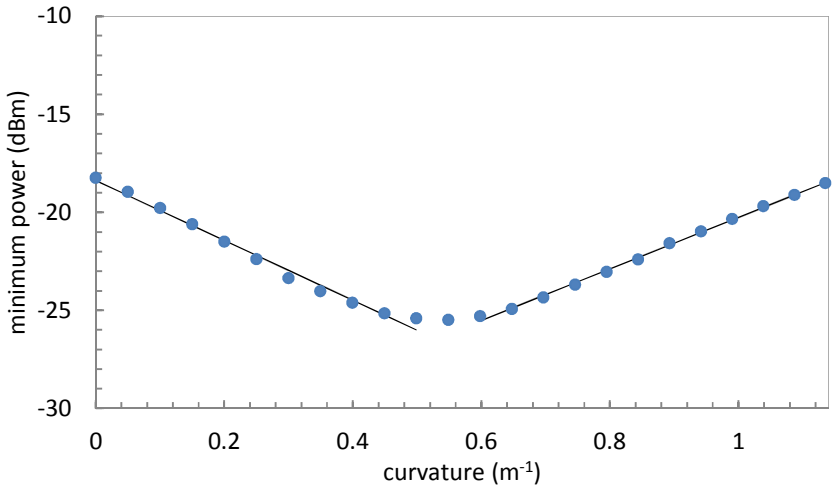

Figure 5.5.6 – Curvature response in power of the interferometric taper 2. Line (linear fit).

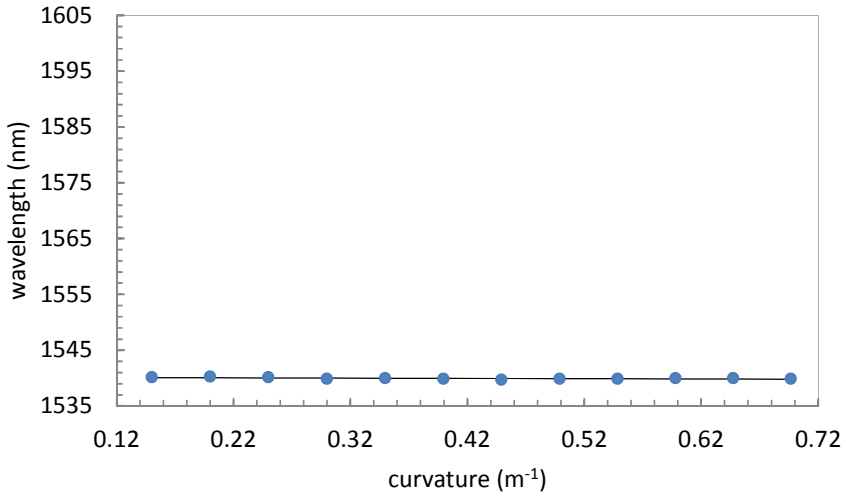

Figure 5.5.7 – Curvature response in wavelength of the interferometric taper 2. Line (linear fit).

Taper 2

		Curvature range (m^{-1})	Curvature sensitivity (dBm/m^{-1})
P_m vs. curvature	Fringe 2	$[0; 0.5]$	-15.27
		$[0.5; 1.1]$	13.14

Table 5 - Summary of all the sensitivities determined for taper 2.

5.6 Conclusion

Taper 1 is a good sensor of temperature, presenting insensitivity to strain and curvature regarding the variation of the wavelengths of the resonant loss peaks. The interference pattern of this interferometer shows some instability during the sensor characterization in temperature, giving rise to two linear regimes for the relation λ_1 versus temperature, one between 25 and 200 ℃ and another from 375 and 500 ℃. The sensitivities are 65 pm/℃ and 151 pm/℃. The estimated variations in temperature resulting from applied strain and curvature are larger in the range of temperatures from 25 to 200 ℃ and equal to 0.02 ℃/με and 20 ℃/ m^{-1}, respectively. In the range comprehending higher temperatures, these variations are found to be 0.006 ℃/με and 8℃/m^{-1}, clearly smaller than the ones registered for lower temperatures. Strain sensing can be performed resorting to the relation between minimum power and strain. The sensitivity is 0.0039 dBm/με, between 0 and 1500 με.

Taper 2 is an even better sensor of temperature, presenting a considerable insensitivity to both strain and curvature regarding the variation of the wavelengths of the resonant loss peaks. For all the fringes analyzed, linear regimes are verified for a wide range of temperatures, between 25 and 510 ℃ for the two fringes associated to shorter wavelengths, and between 25 and 450 ℃ for the fringe associated to the longest wavelength. The maximum sensitivity is determined for fringe 2 and is equal to 110 pm/℃. A remarkable result comes up when this taper is characterized in strain, since λ_2 ends up being rather insensitive to changes in applied strain. The same conclusion can be withdrawn after testing the response of the taper in curvature, which renders this device a strain and curvature-independent temperature sensor. The estimated variations in temperature resulting from applied strain and curvature are 0.01 ℃/με and 4.55 ℃/ m^{-1}, respectively. To this outstanding characteristic one can add the fact that the temperature sensitivity is larger than the one verified for many tested devices in literature **[11-13; 60]** as well as the large range of temperatures one can cover resorting to this sensor. Strain and curvature sensing can be performed resorting to the relation between minimum power and the external parameter. The sensitivities are 0.0042 dBm/με, between 300 and 1100 με, −15.27 dBm/m^{-1}, between 0 and 0.5 m^{-1}, and 13.14 dBm/m^{-1}, from 0.5 to 1.1 m^{-1}.

Taper 1 and taper 2 exhibit some relevant differences concerning the evolution of the interference pattern. The operating range of temperature obtained for taper 2 continually extends from room temperature to 510 ℃, while taper 1 presents a gap from 200 to 375 ℃ characterized by a weak interference between light in the core and traveling along the cladding that results in the dissolution of the interference fringes. Taper 2 is more insensitive to strain and curvature. Evaluating the dependence of the fringes minimum power on the external parameters, this interferometric device also allows for curvature and strain sensing, as taper 1 only works as a good sensor of applied strain.

6. Concluding remarks

6.1 Conclusion

The main objectives set for this dissertation were successfully accomplished, namely in what concerns the assembly of a fully functional setup for taper fabrication, the understanding gained regarding the interaction between CO_2 laser radiation and the optical fiber, the optimization of the taper fabrication process and the characterization of these devices as sensors of temperature, strain and curvature.

The fabrication of tapers using weights attached to the fiber turned out to be a rewarding experience, revealing the potential of the assembled experimental setup for the production of thin tapers allowing for an effective interaction between light traveling along the core and cladding of the tapered portion of the fiber. The time evolution for the taper length is obtained for different weight masses and a connection between smaller taper waist diameters and deeper interference fringes is established. The power losses are studied and as the fabrication process takes place the average transmitted power decreases. Part of the power losses is associated to reflection at the interface between the unchanged fiber and the tapered region. The fact that the wavelengths of the power loss peaks change during the fabrication process constitutes an encouraging observation that supports the expectations of possibly using tapers as sensors, since during the fabrication process some characteristics of the fiber are being actively changed, such as its refractive index, altering the interference conditions and giving rise to wavelength shifts . Longitudinal asymmetry is a feature common to all the tapers produced using this method; an abrupt transition region at the spot where laser light shines upon the fiber is a constant and can account for the losses due to reflection.

The impact of including motorized stages in the setup for taper fabrication is examined as the three major fabrication parameters, Power Width Modulation (PWM), speed differential (SD) and speed magnitude (SM), are changed, which produces identifiable changes in the tapers transmission spectra and shapes. The longitudinal asymmetry lingers on, even though less conspicuous. A compromise is found between low power losses and sharp transmission spectra with deep fringes setting the values for PWM, SD and SM equal to 25 %, 6 and 14, respectively. The reproducibility of the setup is tested

using these values but seems compromised as the obtained interference patterns, for different tapers, differ significantly.

The fabricated tapers are characterized as sensors of temperature, strain and curvature. One of the tested devices is a good sensor of temperature, presenting a considerable insensitivity to both strain and curvature regarding the variation of the wavelengths of the resonant loss peaks. For all the fringes analyzed, linear regimes are verified for a wide range of temperatures, between 25 and 510 $℃$. The maximum sensitivity is determined for fringe 2 and is equal to 110 $\mathrm{pm}/℃$. λ_2 turns out to be rather insensitive to changes in both applied strain and curvature, which renders this device a strain and curvature-independent temperature sensor. The estimated variations in temperature resulting from applied strain and curvature are 0.01 $℃/\mu\varepsilon$ and 4.55 $℃/$ m^{-1}, respectively. To this outstanding characteristic one can add the fact that the temperature sensitivity is larger than the one verified for many tested devices in literature, as well as the large range of temperatures one can cover resorting to this sensor. Strain and curvature sensing can be performed resorting to the relation between minimum power and the external parameter. The sensitivities are 0.0042 $\mathrm{dBm}/\mu\varepsilon$, between 300 and 1100 $\mu\varepsilon$, 15.27 $\mathrm{dBm}/\mathrm{m}^{-1}$, between 0 and 0.5 m^{-1}, and 13.14 $\mathrm{dBm}/\mathrm{m}^{-1}$, from 0.5 to 1.1 m^{-1}. The reproducibility can also be assessed comparing the results of this characterization for different tapers. Some relevant differences concerning the evolution of the interference patterns are witnessed: the operating ranges for temperature sensing differ; the insensitivity towards strain and curvature is more pronounced for certain tapers.

6.2 Future work

Some open-ended possibilities are left unexplored and their pursuit could prove fruitful in improving the work presented in this dissertation.

- Develop efforts towards a better control over the shape of the tapers, perhaps drawing closer to an adiabatic taper and solving lingering longitudinal asymmetries.

- Use the knowledge and expertise acquired to fabricate tapers in more complex fibers, such as suspended-core fibers, to produce micro and nanowires.

- Study more complex configurations for sensing devices involving tapers.

- Fabricate long period gratings (LPGs) using the assembled setup, changing the LabVIEW routine to synchronize laser shots with the movement of the motorized stages.

Appendices

A. The LabVIEW routine implemented to control the motorized stages allows the change of several fabrication parameters such as the speed assigned to each stage or the length of the taper to be fabricated. The versatility of said routine extends to the possibility of controlling the fabrication of a long period grating (LPG).

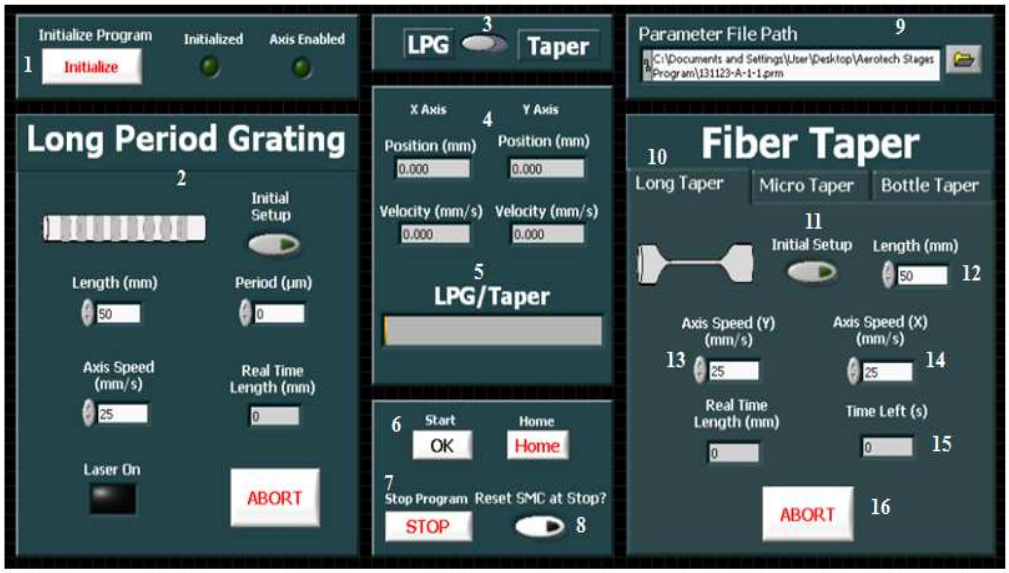

Fig A.1 - Front panel of the LabVIEW routine responsible for setting the taper fabrication parameters.

1. Initialize button – establishing communication with the AEROTECH control unit;
2. LPG menu – changing the parameter values for LPG fabrication;
3. Taper/LPG button – setting the fabrication for either taper or LPG;
4. Information regarding x-axis and y-axis position and velocity;
5. Bar showing the evolution of the fabrication process;
6. Start button – starting fabrication;
7. Stop button – stopping fabrication;
8. Reset SMC at stop button – if activated, when fabrication is interrupted by clicking on the stop button, initialization has to be performed again and the correct initial values are restored.
9. Parameter file path – showing the file that contains the initial values for setup procedures;

10. Long taper/ Micro taper/ Bottle taper – choosing the type of taper to fabricate;
11. Initial Setup button – positioning both stages at the correct initial positions for the type of device one intends to fabricate;
12. Length – setting taper length;
13. Axis speed (Y) – setting the y-stage speed;
14. Axis speed (X) – setting the x-stage speed;
15. Time left – showing the time left until the end of the fabrication process;
16. Abort button – aborting the entire fabrication process.

B. The estimate of the fiber temperature is performed resorting to Stefan-Boltzmann law. A power of 2 W, a 2 mm beam diameter and an emissivity equal to 0.9 (typical of glass) are considered. The laser intensity is given by

$$I = \frac{P}{A} = \frac{2}{\pi(1 \times 10^{-3})^2} = 6.7 \times 10^5 \ \mathrm{W/m^2} \tag{B.1}$$

The temperature T is then estimated through Stefan-Boltzmann law as

$$I = e\sigma T^4 \Leftrightarrow T = \left(\frac{6.7 \times 10^5}{0.9 \times (5.67 \times 10^{-8})}\right)^{1/4} \approx 1600 \ ℃ \tag{B.2}$$

Where e is the emissivity and σ is the Stefan-Boltzmann constant equal to $5.67 \times 10^{-8}\ \mathrm{Wm^{-2}K^{-4}}$.

C. The laser beam diameter d at the focal plane is calculated considering a beam diameter D at the laser output equal to 3.5 mm, an angle divergence θ of 4 mrad and focal length f equal to 100 mm . The diameter d is then obtained through

$$d = \theta \times \mathrm{f} = 4 \ \mathrm{mrad} \times 100 \ \mathrm{mm} = 400 \ \mu\mathrm{m} \tag{C.1}$$

References

1. B. S. Kawasaki, K. O. Hill, R. G. Lamont, *Biconical-taper single-mode fiber coupler,* Optics Letters **6** (1981) 327-328.

2. K. P. Jedrzejewski, F. Martinez, J. D. Minelly, C. D. Hussey, F. P. Payne, *Tapered-beam expander for single-mode optical-fibre gap devices,* Electronics Letters **22** (1986) 105-106.

3. A. C. Boucouvalas, G. Georgiou, E*xternal refractive-index response of tapered coaxial couplers,* Optics Letters **11** (1986) 257-259.

4. F. P. Payne, T. Finegan, M. S. Yataki, R. J. Mears, C.D. Hussey, *Dependence of fused taper couplers on external refractive index,* Electronic Letters **22** (1986) 1207-1209.

5. R. G. Lamont, D. C. Johnson, K. O. Hill, *Power transfer in fused biconical-taper single-mode fiber couplers: dependence on external refractive index,* Applied Optics **24** (1985) 327-332.

6. K. C. Byron, K. Sugden, T. Brichenko, I. Bennion, *Fabrication of chirped Bragg gratings in photosensitive fibre,* Electronics Letters **29** (1993) 1659-1660.

7. L. Dong, J. L. Cruz, L. Reekie, J. A. Tucknott, *Chirped fiber Bragg gratings fabricated using etched tapers,* Optical Fiber Technology **1** (1995) 363-368.

8. M. G. Xu, L. Dong, L. Reekie, J. A. Tucknott, J. L. Cruz, *Temperature-independent strain sensor using a chirped Bragg grating in a tapered optical fibre,* Electronics Letters **31** (1995) 823-825.

9. V. Bhatia, D. Campbell, R. O. Claus, A. M. Vengsarkar, *Simultaneous strain and temperature mesurement with long-period gratings,* Optics Letters **22** (1997) 648-650.

10. O. Frazão, M. Melo, P. V. S. Marques, J. L. Santos, *Chriped Bragg grating fabricated in fused fibre taper for strain-tamperature discrimination,* Measurement Science and Technology **16** (2005) 984-988.

11. O. Frazão, L. M. Marques, S. Santos, J. M. Baptista, J. L. Santos, *Simultaneous measurement for strain and temperature based on a long-period grating combined with a high-birefringence fiber loop mirror,* IEEE Photonics Technology Letters **18** (2006) 2407-2409.

12. O. Frazão, L. Marques, J. M. Marques, J. M. Baptista, J.L. Santos, *Simple sensing head geometry using fibre Bragg gratings for strain-temperature discrimination*, Optics Communications **29** (2007) 68-71.

13. Q. Yao, H. Meng, W. Wong, H. Xue, R. Xiong, B. Huang, C. Tan, X. Huang, *Simultaneous measurement of refractive index and temperature based on a core-offset Mach-Zehnder interferometer combined with a fiber Bragg gratings*, Sensors and Actuators A: Physical **209** (2014) 73-77.

14. T. A. Birks, Y. W. Li, *The shape of fiber tapers*, Journal of Lightwave Technology **10** (1992) 432-438.

15. T. E. Dimmick, G. Kakarantzas, T. A. Birks, P. J. Russel, *Carbon dioxide laser fabrication of fused-fiber couplers and tapers*, Applied Optics **38** (1999) 6845-6848.

16. Y. Li, L.Chen, E. Harris, X. Bao, *Double-Pass in-line fiber taper Mach-Zehnder interferometer sensor*, IEEE Photonics Technology Letters **22** (2010) 1750-1752.

17. Z. Tian, S. S.-H. Yam, J. Barnes, W. Bock, P. Greig, J. M. Fraser, H.-P. Loock, R. D. Oleschuk, *Refractive index sensing with Mach-Zehnder interferometer based on concatenating two single-mode fiber tapers*, IEEE Photonics Technology Letters **20** (2008) 626-628.

18. H. Gong, Z. Qian, X. Yang, C.-L. Zhao, X. Dong, *Optical fiber inclinometer based on a fiber taper cascading a peanut-shape structure*, IEEE Sensors Journal **15** (2015) 3917-3920.

19. G. Yin, S. Lou, K. Zou, *Refractive index sensor with asymmetrical fiber Mach-Zehnder interferometer based on concatenating single-mode abrupt taper and core-offset section*, Optics & Laser Technology **45** (2013) 294-300.

20. K. C. Kieu, M. Mansuripur, *Biconical Fiber Taper Sensors*, IEEE Photonics Technology Letters **18** (2006) 2239-2241.

21. T. Wei, X. Lan, H. Xiao, *Fiber inline core-cladding-mode Mach-Zehnder interferometer fabricated by two-point CO_2 laser irradiations*, IEEE Photonics Technology Letters **21** (2009) 669-671.

22. D. Monzón-Hernández, A. Martinez-Rios, I. Torres-Gomez, G. Salceda-Delgado, *Compatc optical fiber curvature sensor based on concatenating two tapers*, Optics Letters **36** (2011) 4380-4382.

23. Y. Geng, X. Li, X. Tan, Y. Deng, Y. Yu, *High-sensitivity Mach-Zehnder interferometric temperature fiber sensor based on a waist-enlarged fusion taper*, IEEE Sensors Journal **11** (2011) 2891-2894.

24. L. Niu, C.-L. Zhao, H. Gong, Y. Li, S. Jin, *Curvature sensor based on a two cascading abrupt-tapers modal interferometer in single mode fiber*, Optics Communications **333** (2011) 11-12.

25. R. Yang, Y.-S. Yu, G. Chen, Y. Xue, X.-L. Zhang, J.-C. Guo, C. Wang, F. Zhu, B.-L. Zhang, Q.-D. Chen, H.-B. Sun, *S-tapered fiber sensors for highly sensitive measurement of refractive index and axial strain*, Journal of Lightwave Technology **30** (2012) 3126-3132.

26. M. Deng, D. Liu, D. Li, *Magnetic field sensor based on asymmetric optical fiber taper and magnetic fluid*, Sensors and Actuators A: Physical **211** (2014) 55-59.

27. O. Frazão, P. Caldas, F. M. Araújo, L. A. Ferreira, J. L. Santos, *Optical flowmeter using a modal interferometer based on a single nonadiabatic fiber taper*, Optics Letters **32** (2007) 1974-1976.

28. Z. Tian, S. S.-H. Yam, H.-P. Loock, *Refractive index sensor based on an abrupt taper Michelson interferometer in a single-mode fiber*, Optics Letters **33** (2008) 1105-1107.

29. L. M. N. Amaral, O. Frazão, J. L. Santos, A. B. Lobo Ribeiro, *Fiber-optic inclinometer based on a taper Michelson interferometer*, IEEE Sensors Journal **11** (2011) 1811-1814.

30. L. Yuan, J. Yang, Z. Liu, J. Sun, *In-fiber integrated Michelson interferometer*, Optics Letters **31** (2006) 2692-2694.

31. L. Yuan, J. Yang, Z. Liu, *A compact fiber-optic flow velocity sensor based on a twin-core fiber Michelson interferometer*, IEEE Sensors Journal **8** (2008) 1114-1117.

32. J. Zhang, Q. Sun, R. Liang, J. Wo, D. Liu, P. Shum, *Microfiber Fabry-Pérot interferometer fabricated by taper-drawing technique and its application as a radio frequency interrogated refractive index sensor*, Optics Letters **37** (2012) 2925-2927.

33. T. Allsop, F. Floreani, K. P. Jedrzejewski, P. V. S. Marques, R. Romero, *Spectral characteristics of tapered LPG device as a sensing element of refractive índex and temperature*, Journal of Lightwave Technology **24** (2006) 870-878.

34. O. Frazão, R. Falate, J. L. Fabris, J. L. Santos, L. A. Ferreira, F. M. Araújo, *Optical inclinometer based on a single long-period fiber grating combined with a fused taper*, Optics Letters **31** (2006) 2960-2962.

35. O. Frazão, S. F. O. Silva, A. Guerreiro, J. L. Santos, L. A. Ferreira, F. M. Araújo, *Strain sensitivity control fiber Bragg grating structures with fused tapers*, Applied Optics **46** (2007) 8578-8582.

36. S. Silva, L. Coelho, J. M. Almeida, O. Frazão, J. L. Santos, F. X. Malcata, M. Becker, M. Rothhardt, H. Bartelt, *H_2 sensing based on a Pd-coated tapered-FBG fabricated by DUV femtosecond laser technique*, IEEE Photonics Technology Letters **25** (2013) 401-403.

37. X. Liu, T. Wang, Y. Wu, Y. Gong, Y.-J. Rao, *Dual-parameter sensor based on tapered FBG combined with microfiber cavity*, IEEE Photonics Technology Letters **16** (2014) 817-820.

38. A. Ashkin, *Accelaration and trapping of particles by radiation pressure*, Physical Review Letters **24** (1970) 156-159.

39. A. Ashkin, J. M. Dziedzic, J. E. Biorkholm, S. Chu, *Observation of a single-beam gradient force optical trap for dielectric particles.* Optics Letters **11** (1986) 288-290.

40. D. G. Grier, *A revolution in optical manipulation*, Nature **424** (2003) 21-27.

41. G. Brambilla, G. S. Murugan, J. S. Wilkinson, D. J. Richardson, *Optical manipulation of microspheres along a subwavelength optical wire*, Optics Letters **32** (2007) 2041-3043.

42. G. Brambilla, F. Xu, P. Horak, Y. Jung, F. Koizumi, N. P. Sessions, E. Koukharenko, X. Feng, G. S. Murugan, J. S. Wilkinson, D. J. Richardson, *Optical*

fiber nanowires and microwires: fabrication and applications, Advances in Optics and Photonics **1** (2009) 107-161.

43. J. Villatoro, D. Monzón-Hernández, *Fast detection of hydrogen with nano fiber tapers coated with ultra-thin palladium layers*, Optics Express **13** (2005) 5087-5092.

44. Z. Wei, Z. Song, X. Zhang, Z. Meng, *Microparticle detection with optical microfibers*, IEEE Photonics Technology Letters **25** (2013) 568-571.

45. C. Wuttke, M. Becker, S. Brückner, M. Rothhardt, A. Rauschenbeutel, *Nanofiber Fabry-Pérot microresonator for non-linear optics and cavity quantum electrodynamics*, Optics Letters **37** (2012) 1949-1951.

46. J. D. Love, W. M. Henry, *Quantifying loss minimisation in single-mode fibre tapers*, Electronics Letters **22** (1986) 912-914.

47. J. D. Love, W. M. Henry, W. J. Stewart, R. J. Black, S. Lacroix, F. Conthier, *Tapered single-mode fibers and devices. I. Adiabaticity criteria,* Optoelectronics, IEEE Proceedings J **138** (1991) 343-354.

48. O. Svelto, *Principles of Lasers*, Spinger, 5th edition (2010).

49. J. M. P. Coelho, M. C. Nespereira, M. Abreu, J. M. Rebordão, *Modeling refractive índex change in writing long-period fiber gratings using mid-infrared laser radiation*, Photonic Sensors **3** (2013) 67-73.

50. A. J. C. Grellier, N. K. Zayer, C. N. Pannell, *Heat transfer modelling in* CO_2 *laser processing of optical fibers*, Optics communications **152** (1998) 324-328.

51. H. S. Ryu, Y. Park, S. T. Oh, Y. Chung, D. Y. Kim, *Effect of asymmetric stress relaxation on the polarization-dependent transmission characteristics of a* CO_2 *laser-written long-period fiber grating*, Optics Letters **28** (2003) 155-157.

52. W. Tian, W. K. S. Chiu, *Temperature prediction for* CO_2 *laser heating of moving glass rods*, Optics & Laser Technology **36** (2004) 131-137.

53. S. T. Oh, W. T. Han, U. C. Paek, Y. Chung, *Azimuthally symmetric long-period fiber gratings fabricated with* CO_2 *laser*, Microwave and Optical Technology Letters **41** (2004) 188-190.

54. X. Liu, M. Yan, L. Zhan, S. Luo, Z. Zhang, Y. Xia, *Controlling of symmetric and asymmetric mode coupling in long-period fiber gratings singe-side induced by long-pulse CO_2 laser,* Optics Communications **284** (2011) 1232-1237.

55. A. D. Yablon, M. F. Yan, P. Wisk, F. V. DiMarcello, J. W. Fleming, W. A. Reed, E. M. Monberg, D. J. DiGiovanni, J. Jasapara, *Refractive index perturbations in optical fibers resulting from frozen-in viscoelasticity,* Applied Physics Letters **84** (2004) 19-21.

56. A. D. Yablon, *Optical and mechanical effects of frozen-in stresses and strains in optical fibers,* IEEE Journal of Selected Topics in Quantum Electronics **10** (2004) 300-311.

57. S. T. Yang, M. J. Matthews, S. Elhadj, V. G. Draggoo, S. E. Bisson, *Thermal transport in CO_2 laser irradiated fused silica: in situ measurements and analysis,* Journal of Applied Physics **106** (2009) (103106 – 103106-7).

58. A. Gomes, V. Amorim, *Carruagens Aerotech,* Relatório final da disciplina de Laboratórios de Física III, Faculdade de Ciências da Universidade do Porto, 2013.

59. E. Hecht, *Optics,* Addison Wesley, 4th edition (2002).

60. C. C. Ye, S. W. James, R. P. Tatam, *Simultaneous temperature and bend sensing with long-period fiber gratings,* Optics Letters **25** (2000) 1007-1009.

61. Y.-P. Wang, L. Xiao, D. N. Wang, W. Jin, *Highly sensitive long-period fiber-grating strain sensor with low temperature sensitivity,* Optics Letters **31** (2006) 3414-3416.

62. R. Kritzinger, D. Schmieder, A. Booysen, *Azimuthally symmetric long-period fiber grating fabrication with a TEM_{01}-mode CO_2 laser,* Measurement Science and Technology **20** (2009) 034004 (8pp).

63. H. Xuan, W. Jin, M. Zhang, *CO_2 laser induced long period gratings in optical microfibers,* Optics Express **17** (2009) 21882-90.

64. F. Bayle, J.-P. Meunier, *Efficient fabrication of fused-fiber biconical taper structures by a scanned CO_2 laser beam technique,* Applied Optics **44** (2005) 6402-6411.

65. L. Ç. Özcan, V. Tréanton, F. Guay, R. Kashyap, *Highly symmetric optical fiber tapers fabricated with a CO_2 laser,* IEEE Photonics Technology Letters **19** (2007) 656-658.

66. D. Monzón-Hernández, V. P. Minkovich , J. Villatoro, *High-temperature sensing with tapers made of microstructured optical fiber,* IEEE Photonics Technology Letters **18** (2006) 511-513.

67. K. Ni, T. Li, L. Hu, W. Qian, Q. Zhang, S. Jin, *Temperature-independent curvature sensor based on tapered photonic crystal fiber interferometer,* Optics Communications **285** (2012) 5148-5150.

68. C. Zhang, J. Zhao, C. Miao, Z. Shen, H. Li, M. Zhang, *High-sensitivity all single-mode fiber curvature sensor based on bulge-taper structures modal interferometer,* Optics Communications **336** (2015) 197-201.

69. B.-O. Guan, H.-Y. Tam, X.-M. Tao, X.-Y. Dong, *Simultaneous strain and temperature measurement using a superstructure fiber Bragg grating,* IEEE Photonics Technology Letters **12** (2000) 675-677.

70. L.-Y. Shao, A. Laronche, M. Smietana, P. Mikulic, W. J. Bock, J. Albert, *Highly sensitive bend sensor with hybrid long-period and tilted fiber Bragg grating,* Optics Communications **283** (2010) 2690-2694.

71. C. Gouveia, P. A. S. Jorge, J. M. Baptista, O. Frazão, *Temperature-independent curvature sensor using FBG cladding modes based on a core misaligned splice,* IEEE Photonics Technology Letters **23** (2011) 804-806.

72. S. Silva, O. Frazão, J. Viegas, L. A. Ferreira, F. M. Araújo, F. X. Malcata, J. L. Santos, *Temperature and strain-independent curvature sensor based on a singlemode/multimode fiber optic structure,* Measurement Science and Technology **22** (2011) 085201 (6pp).

73. M. Deng, L.-P. Tang, T. Zhu, Y.-J. Rao, *Highly sensitive bend sensor based on Mach-Zehnder interferometer using photonic crystal fiber,* Optics Communications **284** (2011) 2849-2853.

74. H. Gong, H. Song, X. Li, J. Wang, X. Dong, *An optical fiber curvature sensor based on photonic crystal fiber modal interferometer,* Sensors and Actuators A: Physical **195** (2013) 139-141.